



# Effects of shear stiffness, rotatory and axial inertia, and interface stiffness on free vibrations of a two-layer beam

Stefano Lenci\*, Francesco Clementi

Department of Civil and Buildings Engineering, and Architecture, Polytechnic University of Marche, Via Brecce Bianche, I-60131 Ancona, Italy

## ARTICLE INFO

### Article history:

Received 26 December 2011

Received in revised form

2 July 2012

Accepted 4 July 2012

Handling Editor: S. Ilanko

Available online 1 August 2012

## ABSTRACT

The linear dynamics of a two-layer beam is considered. Each beam is modelled by the Timoshenko kinematics, and all inertia terms are considered. The interface allows normal and tangential detachments, which are linearly proportional to the transmitted stresses. The eigenvalue problem providing the natural frequencies is solved exactly.

An extensive study of the natural frequencies and of the normal modes is performed with the aim of understanding how the mechanical parameters of the composite influence the vibration behaviour.

The study of the convergence of the solution toward that of a simplified problem obtained by neglecting axial and rotational inertia, shear deformations and by considering interface perfect adherence in the normal direction, constitutes the second objective of the work. This permits to consciously assess when these mechanical terms can actually be neglected, contrarily to what is usually done in practice, where they are disregarded 'a priori', without adequate care.

© 2012 Elsevier Ltd. All rights reserved.

## 1. Introduction

Laminated composites, and more generally multilayered beams, are mainly designed for engineering applications where both high strength-to-weight and stiffness-to-weight ratios are required. One of the main advantages is that, by properly combining different layers of different materials, they can be designed according to specific requirements, leading to the so called 'multifunctional' composites [1], where each layer is devoted to a specific performance (not only structural strength and stiffness, but also thermal insulation, dissipation, etc.). Due to this and other characteristics, they are widely used in aerospace, automotive industry, microelectronics engineering, naval engineering, civil engineering, etc.

The use of laminates requires careful mechanical analysis in order to accurately predict the response to external loads. In particular, composite beam structures often operate in complex environmental conditions and are frequently exposed to a variety of dynamic excitations. Thus, the knowledge of their natural frequencies is very important to avoid resonance phenomena. Therefore, we focus on their accurate determination, since they are critical in design [2].

Historically, however, the static behaviour of laminates has been studied first, by taking into account only the relative slip between layers, which is a key behaviour. The first formulation for composite beams with weak interface is reported in [3] and uses the Euler–Bernoulli kinematics. Subsequent contributions took into account shear deformability of layers according to the well-known Timoshenko theory [4,5].

\* Corresponding author.

E-mail addresses: [lenci@univpm.it](mailto:lenci@univpm.it) (S. Lenci), [francesco.clementi@univpm.it](mailto:francesco.clementi@univpm.it) (F. Clementi).

Later, these different kinematics models have been used in the dynamical framework, too, the former for example in [2,6–8] and the latter for example in [8–11]. Actually, the free dynamics behaviour of two-layer beams has been largely studied in the literature [12–20], where numerical [21,22], analytical/theoretical [8,23] as well as experimental [8,11,24,25] studies can be found. Also some specific issues have been investigated, such as, the effect of interface damage [8,26,27], the viscoelastic behaviour of the core [28–30], the effect of the temperature [31,32], the lateral–torsional vibration coupling [33], curved beams [34], and boundary conditions effects [35].

In this paper, we consider the model used in [9] and in Section 5 of [8], i.e., a shear-deformable two-layer beam with elastic interface and with all inertia terms: axial, rotational (which are not commonly considered) and transverse. We also consider both tangential (slip) and normal (detachment, or uplift) interface stiffnesses, and we mainly focus on transversal (or flexural) vibrations, because they are the most important in applications.

We have two main goals. The first consists of a detailed parametric study of the natural frequencies, which is aimed at highlighting their dependence on the shear deformability, axial and rotational inertia, and interface stiffness of the two-layer beam. Furthermore, we study the associated mode shapes, and we highlight the presence of ‘strange’ or ‘uncommon’ modes (e.g., shearing modes), of internal resonances and of the veering phenomenon.

The second goal consists of verifying the reliability of a simplified model, which (i) neglects shear deformability (i.e., it considers Euler–Bernoulli beams), (ii) neglects axial and rotational inertia, and (iii) consider interface perfect adherence in the normal direction. This model is much more simple (for example, it has only two parameters instead of 14) and can be used in every day computations, while the full model, although can be solved in closed form, cannot be handled easily since, for example, it requires the solution of a transcendental equation of order 12 with no well-separated roots. It is commonly used in the literature (see for example [36]), although the practical validity of the underlying hypotheses is not always clear. Thus, we perform extensive computations in order to check its reliability. As a by-product, we obtain information on the parameters redundancy of the full model.

The paper is organised as follows. In Section 2 we describe the mechanical model, the governing equations and we obtain their dimensionless version, which are the starting point of subsequent developments. In Section 3 we study the wave propagation problem of both the general and the simplified problems, obtaining the dispersion curves, which are used in the following sections. Section 4 constitutes the core of the paper, where the natural frequencies are computed and the main results are obtained. It is worth to remark that, although the mathematical problem governing the mechanical behaviour has infinite eigenvalues, attention is mainly paid to the lowest ones, since it is known that beam theories, even refined, are inaccurate for high order natural frequencies, where, e.g., thickness effects become important. The paper ends with some conclusions and suggestions for further developments (Section 5).

## 2. Problem formulation

We consider the two-layer beam illustrated in Fig. 1 having an elastic interface with normal and tangential elastic stiffness.

Each layer is assumed to behave like a Timoshenko shear-deformable beam. In the static case the same assumption has been used in [5]. Accordingly, the field equations are (see Fig. 1):

Balance:

$$\begin{cases} N'_1 - F_T = \rho_1 \widetilde{A}_1 \ddot{w}_1, \\ T'_1 - F_N = \rho_1 A_1 \ddot{v}_1, \\ M'_1 - T_1 + \hat{h}_1 F_T = \rho_1 J_1 \ddot{\theta}_1, \end{cases} \quad \begin{cases} N'_2 + F_T = \rho_2 \widetilde{A}_2 \ddot{w}_2, \\ T'_2 + F_N = \rho_2 A_2 \ddot{v}_2, \\ M'_2 - T_2 + \hat{h}_2 F_T = \rho_2 J_2 \ddot{\theta}_2. \end{cases} \quad (1)$$

Compatibility:

$$\begin{cases} \varepsilon_1 = \hat{w}'_1, \\ \gamma_1 = \hat{v}'_1 + \theta_1, \\ k_1 = \theta'_1, \end{cases} \quad \begin{cases} \varepsilon_2 = \hat{w}'_2, \\ \gamma_2 = \hat{v}'_2 + \theta_2, \\ k_2 = \theta'_2. \end{cases} \quad (2)$$

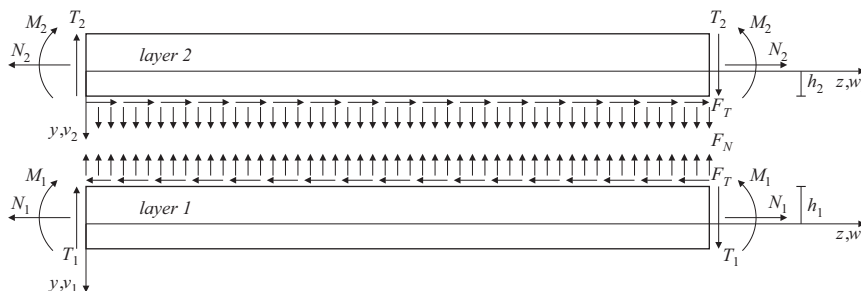


Fig. 1. The two-layer beam.

Constitutive relations:

$$\begin{cases} N_1 = E_1 A_1 \varepsilon_1, \\ T_1 = \chi_1 G_1 A_1 \gamma_1, \\ M_1 = E_1 J_1 k_1, \end{cases} \quad \begin{cases} N_2 = E_2 A_2 \varepsilon_2, \\ T_2 = \chi_2 G_2 A_2 \gamma_2, \\ M_2 = E_2 J_2 k_2. \end{cases} \quad (3)$$

Interface:

$$\begin{cases} \hat{s}_T = \hat{w}_1 - \hat{w}_2 - \hat{h}_1 \theta_1 - \hat{h}_2 \theta_2, \\ \hat{s}_N = \hat{v}_1 - \hat{v}_2, \end{cases} \quad \begin{cases} F_T = \hat{k}_T \hat{s}_T, \\ F_N = \hat{k}_N \hat{s}_N. \end{cases} \quad (4)$$

Before proceeding further it is worth to remark that the interface constitutive assumption (4)<sub>2,4</sub> allows for interpenetration between the two beams, i.e.,  $\hat{s}_N < 0$ . At a first glance this sound unrealistic. However, in practical applications the interface is usually made of a small interphase strip (e.g., the PVB in structural glasses, the studs in steel–concrete beams, etc.), which is only approximated by the no-thickness model. The compression of this interphase then allows for negative values of  $\hat{s}_N < 0$ . This is of course true only up to certain vibrations amplitude extent, above which nonlinear phenomena occurs. Since we are dealing with (linear) small oscillations, we assume that this threshold is not overcame.

Eqs. (1)–(4) are a differential-algebraic system (DAE) of 22 equations in the 22 unknowns  $N_i, T_i, M_i, \varepsilon_i, \gamma_i, k_i, \hat{w}_i, \hat{v}_i, \theta_i, i = \{1, 2\}; \hat{s}_T, \hat{s}_N, F_T$  and  $F_N$ . All are functions of space,  $\hat{z} \in [0, L]$  ( $L$  is the length of the beam), and of time,  $\hat{t} \in [0, \infty[$ . Prime denotes derivative with respect to  $\hat{z}$ , dot derivative with respect to  $\hat{t}$ .

The 16 parameters of the previous systems are ( $i = \{1, 2\}$ )

- $\widetilde{\rho_i A_i}$ , the mass per unit length involved in the axial inertia;
- $\rho_i A_i$ , the mass per unit length involved in the transversal inertia;
- $\rho_i J_i$ , the second moment of inertia per unit length involved in the rotatory (or rotational) inertia;
- $E_i A_i$ , the axial stiffnesses;
- $\chi_i G_i A_i$ , the shear stiffnesses;
- $E_i J_i$ , the bending stiffnesses;
- $\hat{h}_i$ , the distances of the centroids of the beams from the common interface;
- $\hat{k}_T$  and  $\hat{k}_N$ , the interface stiffnesses in the normal and tangential directions, respectively.

Note that in general  $\widetilde{\rho_i A_i}$  and  $\rho_i A_i$  are equal. However, they appear in different inertia terms, and they have a different mechanical meaning; thus, they will be kept distinct. Actually, we are interested in detecting when the axial inertia  $\rho_i A_i \dot{\hat{w}}_i$ , but not the transverse inertia  $\rho_i A_i \ddot{\hat{v}}_i$ , are negligible, which mathematically entails assuming  $\widetilde{\rho_i A_i} = 0$ .

Each beam and the interface are assumed to be homogeneous, i.e., the previous parameters are  $\hat{z}$ -independent. The beams are not assumed to be isotropic; in fact, the beam parameters can accommodate, up to a certain extent, the anisotropy of the layers. Since there is no coupling between tangential and normal behaviour, the interface is assumed to be orthotropic.

In this paper we consider the case in which both layers are free at the ends, namely

$$N_i = 0, \quad T_i = 0 \quad \text{and} \quad M_i = 0 \quad \text{at} \quad \hat{z} = 0 \quad \text{and} \quad \hat{z} = L. \quad (5)$$

By eliminating compatibility equations, constitutive relations and interfaces equations we obtain

$$\begin{cases} E_1 A_1 \hat{w}_1'' - \hat{k}_T \hat{s}_T = \widetilde{\rho_1 A_1} \ddot{\hat{w}}_1, \\ \chi_1 G_1 A_1 (\hat{v}_1' + \theta_1)' - \hat{k}_N \hat{s}_N = \rho_1 A_1 \ddot{\hat{v}}_1, \\ E_1 J_1 \theta_1'' - \chi_1 G_1 A_1 (\hat{v}_1' + \theta_1) + \hat{h}_1 \hat{k}_T \hat{s}_T = \rho_1 J_1 \ddot{\theta}_1, \end{cases} \quad \begin{cases} E_2 A_2 \hat{w}_2'' + \hat{k}_T \hat{s}_T = \widetilde{\rho_2 A_2} \ddot{\hat{w}}_2, \\ \chi_2 G_2 A_2 (\hat{v}_2' + \theta_2)' + \hat{k}_N \hat{s}_N = \rho_2 A_2 \ddot{\hat{v}}_2, \\ E_2 J_2 \theta_2'' - \chi_2 G_2 A_2 (\hat{v}_2' + \theta_2) + \hat{h}_2 \hat{k}_T \hat{s}_T = \rho_2 J_2 \ddot{\theta}_2, \end{cases} \quad \begin{cases} \hat{s}_T = \hat{w}_1 - \hat{w}_2 - \hat{h}_1 \theta_1 - \hat{h}_2 \theta_2, \\ \hat{s}_N = \hat{v}_1 - \hat{v}_2. \end{cases} \quad (6)$$

Instead of dealing with the previous equations, it is useful to consider dimensionless equations and parameters. Thus, we define

$$\hat{z} = Lz, \quad \hat{w}_i = Lw_i, \quad \hat{v}_i = Lv_i, \quad \hat{h}_i = Lh_i, \quad \hat{s}_T = Ls_T, \quad \hat{s}_N = Ls_N, \quad \hat{t} = L^2 \sqrt{\frac{\rho_1 A_1}{E_1 J_1}} t, \quad (7)$$

where  $z \in [0, 1]$  is the dimensionless space variable and  $t \in [0, \infty[$  is the dimensionless time. Eqs. (6) then become

$$\begin{cases} \mu_1 w_1'' - k_T s_T = \varrho_1 \ddot{w}_1, \\ \eta_1 (v_1' + \theta_1)' - k_N s_N = \ddot{v}_1, \\ \theta_1'' - \eta_1 (v_1' + \theta_1) + h_1 k_T s_T = \zeta_1 \ddot{\theta}_1, \\ \mu_2 w_2'' + k_T s_T = \varrho_2 \ddot{w}_2, \\ \eta_2 (v_2' + \theta_2)' + k_N s_N = \beta \ddot{v}_2, \\ \alpha \theta_2'' - \eta_2 (v_2' + \theta_2) + h_2 k_T s_T = \zeta_2 \ddot{\theta}_2, \\ s_T = w_1 - w_2 - h_1 \theta_1 - h_2 \theta_2, \\ s_N = v_1 - v_2, \end{cases} \quad (8)$$

and the 14 dimensionless parameters are now ( $i = \{1, 2\}$ )

- $\varrho_i = \widetilde{\rho_i A_i} / \rho_1 A_1$ , the mass per unit length in the axial inertia;
- $\eta_i = L^2 (\chi_i G_i A_i / E_1 J_1)$ , the shear stiffnesses;
- $\zeta_i = \rho_i J_i / L^2 \rho_1 A_1$ , the rotational inertia;
- $\mu_i = L^2 (E_i A_i / E_1 J_1)$ , the axial stiffnesses;
- $h_i = \hat{h}_i / L$ , the interface-centroids distances;
- $k_T = \hat{k}_T (L^4 / E_1 J_1)$  and  $k_N = \hat{k}_N (L^4 / E_1 J_1)$ , the tangential and normal interface stiffnesses;
- $\alpha = E_2 J_2 / E_1 J_1$  and  $\beta = \rho_2 A_2 / \rho_1 A_1$ .

Note that in principle one should have  $\zeta_1 = 1/\mu_1$  and  $\zeta_2 = \alpha\beta/\mu_2$ , but we do not make these simplifications since in classical beam theories the axial stiffness is considered as a unique parameter, and not as the product of  $E_i$  and  $A_i$  (the same for the bending stiffness).

The boundary conditions (5) associated to Eqs. (8) become

$$\begin{aligned} w_1'(0) &= 0, & w_1'(1) &= 0, \\ w_2'(0) &= 0, & w_2'(1) &= 0, \\ v_1'(0) + \theta_1(0) &= 0, & v_1'(1) + \theta_1(1) &= 0, \\ v_2'(0) + \theta_2(0) &= 0, & v_2'(1) + \theta_2(1) &= 0, \\ \theta_1'(0) &= 0, & \theta_1'(1) &= 0, \\ \theta_2'(0) &= 0, & \theta_2'(1) &= 0. \end{aligned} \quad (9)$$

Our aim is to detect the effects of  $\varrho_1$ ,  $\varrho_2$ ,  $\eta_1$ ,  $\eta_2$ ,  $\zeta_1$ ,  $\zeta_2$  and  $k_N$  on the natural frequencies of the two-layer beam. More precisely, we are interested in detecting when the natural frequencies practically reaches the theoretical limits for  $\varrho_1 \rightarrow 0$ ,  $\varrho_2 \rightarrow 0$ ,  $\eta_1 \rightarrow \infty$ ,  $\eta_2 \rightarrow \infty$ ,  $\zeta_1 \rightarrow 0$ ,  $\zeta_2 \rightarrow 0$  and  $k_N \rightarrow \infty$ .

### 2.1. The simplified problem

The limit  $k_N \rightarrow \infty$  implies that  $v_1 = v_2 = v$ ;  $\eta_1 \rightarrow \infty$  implies that  $\theta_1 = -v_1' = -v'$ ;  $\eta_2 \rightarrow \infty$  implies that  $\theta_2 = -v_2' = -v'$ . Therefore, in the simplified case the problem (8) becomes

$$\begin{cases} \mu_1 w_1'' - k_T s_T = 0, \\ \mu_2 w_2'' + k_T s_T = 0, \\ (1 + \alpha)v'''' + (1 + \beta)\ddot{v} - h k_T s_T' = 0, \\ s_T = w_1 - w_2 + h v', \end{cases} \quad (10)$$

where  $h = h_1 + h_2$ . In (10) the unknowns are three ( $s_T$  can be easily eliminated from the equations) and the parameters are six ( $\alpha$ ,  $\beta$ ,  $\mu_1$ ,  $\mu_2$ ,  $k_T$  and  $h$ ).

Eliminating  $w_i$  from (10) yields

$$\begin{cases} s_T'' = k_T s_T \left( \frac{1}{\mu_1} + \frac{1}{\mu_2} \right) + h v''', \\ (1 + \alpha)v'''' + (1 + \beta)\ddot{v} - h k_T s_T' = 0, \end{cases} \quad (11)$$

which can be further reduced to the single equation:

$$s_T'''' - \delta_1 s_T''' + \delta_3 s_T'' - \delta_2 \delta_3 s_T' = 0, \quad (12)$$

where there are only the three parameters

$$\delta_1 = k_T \left( \frac{1}{\mu_1} + \frac{1}{\mu_2} + \frac{h^2}{1+\alpha} \right), \quad \delta_2 = k_T \left( \frac{1}{\mu_1} + \frac{1}{\mu_2} \right), \quad \delta_3 = \frac{1+\beta}{1+\alpha}. \quad (13)$$

Note that  $\nu$  satisfy exactly the same equation.

By rescaling the time by a factor  $1/\sqrt{\delta_3}$ , we see from (12) that the parameter  $\delta_3$  can be eliminated, so that the parameters of the simplified problem are actually only two.

In this simplified case, the boundary conditions (5) can be rewritten in the form

$$\begin{aligned} s'_T(0) &= 0, & s'_T(1) &= 0, \\ s''_T(0) &= \delta_1 s_T(0), & s''_T(1) &= \delta_1 s_T(1), \\ s''''_T(0) &= \delta_1 s'''_T(0), & s''''_T(1) &= \delta_1 s'''_T(1), \end{aligned} \quad (14)$$

and must be associated to Eq. (12).

### 3. Wave propagation

We initially study the wave propagation properties by determining the dispersion condition [37] for the considered layered beam.

Let us assume

$$\begin{aligned} w_1 &= c_1 e^{i(kz + \omega t)}, \\ v_1 &= c_2 e^{i(kz + \omega t)}, \\ \theta_1 &= c_3 e^{i(kz + \omega t)}, \\ w_2 &= c_4 e^{i(kz + \omega t)}, \\ v_2 &= c_5 e^{i(kz + \omega t)}, \\ \theta_2 &= c_6 e^{i(kz + \omega t)}. \end{aligned} \quad (15)$$

Inserting the expressions (15) in the governing Eqs. (8), and eliminating  $e^{i(kz + \omega t)}$ , we obtain the system  $(\mathbf{A} + \omega^2 \mathbf{B})\mathbf{x} = \mathbf{0}$ , where  $\mathbf{x}^T = [c_1, c_2, c_3, c_4, c_5, c_6]$  and where the self-adjoint matrix  $\mathbf{A} = \mathbf{A}(k)$  is given by

$$\begin{bmatrix} -\mu_1 k^2 - k_T & 0 & h_1 k_T & k_T & 0 & h_2 k_T \\ 0 & -\eta_1 k^2 - k_N & i\eta_1 k & 0 & k_N & 0 \\ h_1 k_T & -i\eta_1 k & -\eta_1 k^2 - h_1^2 k_T & -h_1 k_T & 0 & -h_1 k_T h_2 \\ k_T & 0 & -h_1 k_T & -\mu_2 k^2 - k_T & 0 & -h_2 k_T \\ 0 & k_N & 0 & 0 & -\eta_2 k^2 - k_N & i\eta_2 k \\ h_2 k_T & 0 & -h_1 k_T h_2 & -h_2 k_T & -i\eta_2 k & -\eta_2 k^2 - h_2^2 k_T - \alpha k^2 \end{bmatrix}, \quad (16)$$

while the diagonal matrix  $\mathbf{B}$  is given by

$$\begin{bmatrix} \varrho_1 & 0 & 0 & 0 & 0 & 0 \\ 0 & 1 & 0 & 0 & 0 & 0 \\ 0 & 0 & \zeta_1 & 0 & 0 & 0 \\ 0 & 0 & 0 & \varrho_2 & 0 & 0 \\ 0 & 0 & 0 & 0 & \beta & 0 \\ 0 & 0 & 0 & 0 & 0 & \zeta_2 \end{bmatrix}. \quad (17)$$

The system has a nontrivial solution if and only if  $\det(\mathbf{A} + \omega^2 \mathbf{B}) = 0$ . The solutions provide the dispersion relations  $k = k(\omega)$ .

The previous one is a nonlinear algebraic equation containing only even powers of  $k$  up to  $k^{12}$ . Thus, it is an equation of the sixth order in  $k^2$ . This means that there are at most six waves propagating at the same frequency (but in general with different velocities, since the velocity is given by  $c = k/\omega$ ).

An example is reported in Fig. 2. There are various branches, up to six, with crossing as well as veering points. There are also four cut-off frequencies, above which new waves can propagate. This clearly shows how complicated is the wave propagation problem for the two-layer beam.

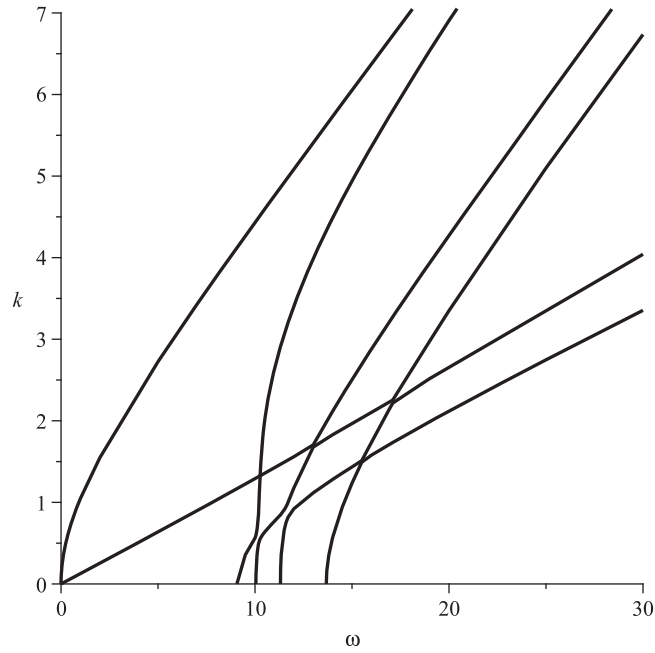


**Fig. 2.** The dispersion relations  $k = k(\omega)$  for  $\varrho_1 = 0.2$ ,  $\varrho_2 = 0.3$ ,  $\eta_1 = 10$ ,  $\eta_2 = 14$ ,  $\zeta_1 = 0.1$ ,  $\zeta_2 = 0.11$ ,  $\mu_1 = 15$ ,  $\mu_2 = 16$ ,  $h_1 = 0.04$ ,  $h_2 = 0.05$ ,  $k_T = 10$ ,  $k_N = 100$ ,  $\alpha = 1.1$ ,  $\beta = 1.15$ .

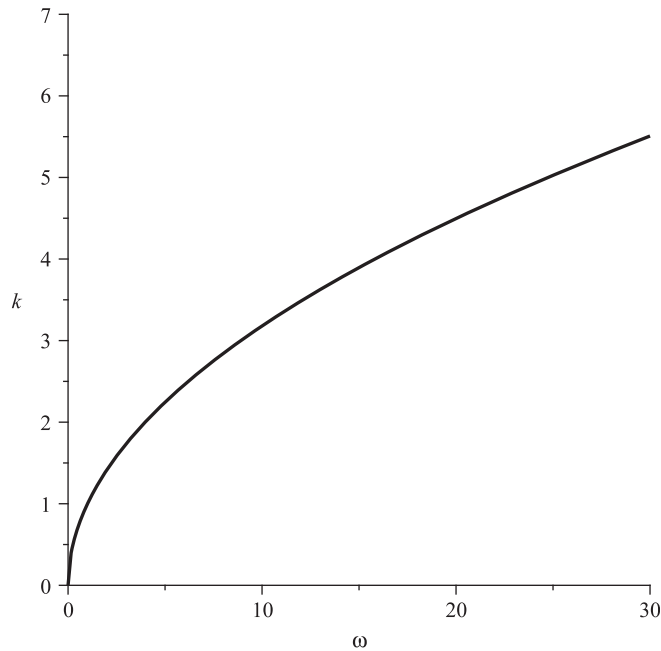


**Fig. 3.** The dispersion relation  $k = k(\omega)$  in the simplified problem for  $\mu_1 = 15$ ,  $\mu_2 = 16$ ,  $h_1 = 0.04$ ,  $h_2 = 0.05$ ,  $k_T = 10$ ,  $\alpha = 1.1$ ,  $\beta = 1.15$ , namely for  $\delta_1 = 1.3302$ ,  $\delta_2 = 1.2917$  and  $\delta_3 = 1.0238$ .

### 3.1. The simplified problem

In the simplified problem (12) we assume  $s_T = e^{i(kz + \omega t)}$  and obtain the characteristic equation

$$k^6 - \delta_1 k^4 - \delta_3 \omega^2 k^2 + \delta_2 \delta_3 \omega^2 = 0, \quad (18)$$

which is a third order equation in  $k^2$ , so that we have at maximum three propagating waves for each value of  $\omega$ . Actually, by the Descartes' rule of sign it is possible to see that there is at most one positive solution  $u = k^2$  of (18), namely only one

wave can propagate. It is reported in Fig. 3 for the same values of the parameters of Fig. 2. Comparing these two figures it is immediate to ascertain how much more complicated is the situation in the original problem.

#### 4. Vibrations

To determine the natural frequencies of the vibrating two-layer beam we assume

$$\begin{aligned}w_1(z,t) &= W_1(z) e^{i\omega t}, \\v_1(z,t) &= V_1(z) e^{i\omega t}, \\\theta_1(z,t) &= \Theta_1(z) e^{i\omega t}, \\w_2(z,t) &= W_2(z) e^{i\omega t}, \\v_2(z,t) &= V_2(z) e^{i\omega t}, \\\theta_2(z,t) &= \Theta_2(z) e^{i\omega t},\end{aligned}\tag{19}$$

so that the system (8) becomes

$$\begin{cases} \mu_1 W_1'' - k_T S_T + \varrho_1 \omega^2 W_1 = 0, \\ \eta_1 (V_1' + \Theta_1)' - k_N S_N + \omega^2 V_1 = 0, \\ \Theta_1'' - \eta_1 (V_1' + \Theta_1) + h_1 k_T S_T + \zeta_1 \omega^2 \Theta_1 = 0, \end{cases}$$

$$\begin{cases} \mu_2 W_2'' + k_T S_T + \varrho_2 \omega^2 W_2 = 0, \\ \eta_2 (V_2' + \Theta_2)' + k_N S_N + \beta \omega^2 V_2 = 0, \\ \alpha \Theta_2'' - \eta_2 (V_2' + \Theta_2) + h_2 k_T S_T + \zeta_2 \omega^2 \Theta_2 = 0, \end{cases}$$

$$\begin{cases} S_T = V_1 - V_2 - h_1 \Theta_1 - h_2 \Theta_2, \\ S_N = V_1 - V_2. \end{cases}\tag{20}$$

To look for the solution of (20) we proceed as follows.

- Fix a value of  $\omega$ .
- Find the 12 solutions  $k_1, \dots, k_{12}$  of the dispersion equation  $\det(\mathbf{A} + \omega^2 \mathbf{B}) = 0$  (see Section 3).
- For each value of  $k_i$  solve the problem  $(\mathbf{A} + \omega^2 \mathbf{B})\mathbf{x} = \mathbf{0}$  and, for that  $k_i$ , determine  $c_2 = v_{i2}c_1$ ,  $c_3 = v_{i3}c_1$ ,  $c_4 = v_{i4}c_1$ ,  $c_5 = v_{i5}c_1$  and  $c_6 = v_{i6}c_1$ .
- At this point the general solution of (20) is given by

$$\begin{aligned}W_1(z) &= \sum_{j=1}^{12} d_j e^{(ik_j z)}, \\V_1(z) &= \sum_{j=1}^{12} d_j v_{j2} e^{(ik_j z)}, \\\Theta_1(z) &= \sum_{j=1}^{12} d_j v_{j3} e^{(ik_j z)}, \\W_2(z) &= \sum_{j=1}^{12} d_j v_{j4} e^{(ik_j z)}, \\V_2(z) &= \sum_{j=1}^{12} d_j v_{j5} e^{(ik_j z)}, \\\Theta_2(z) &= \sum_{j=1}^{12} d_j v_{j6} e^{(ik_j z)}.\end{aligned}\tag{21}$$

Note that up to here the procedure is valid for every boundary conditions.

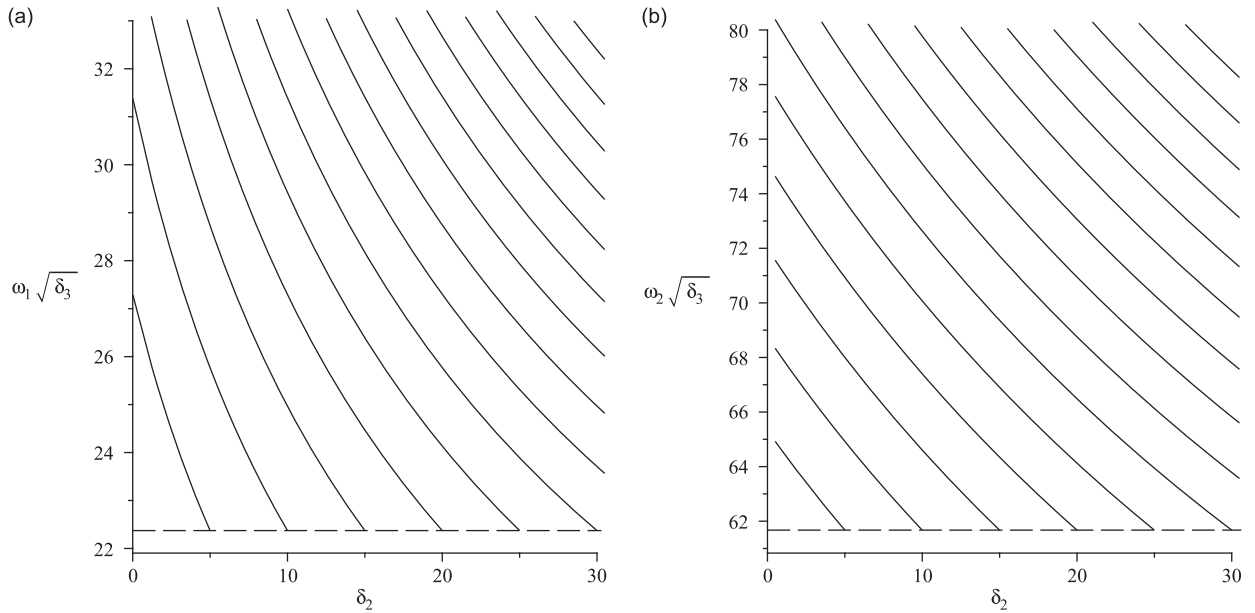


**Fig. 4.** Contour plot of (a) the first and (b) the second natural frequencies as a function of  $\delta_2$  for  $\delta_1 = 5$  (lower left curve), 10, 15, ..., 70, 75 (upper right curve). Note that  $\delta_1 \geq \delta_2 > 0$ ; this shows why the curves end, in the dashed lines, in points where  $\delta_1 = \delta_2$ .

- Impose the 12 boundary conditions to obtain a system of 12 linear equations in the 12 unknown coefficients  $d_1, \dots, d_{12}$ . Let  $\mathbf{C}\mathbf{d} = \mathbf{0}$  be the matrix form of this linear homogeneous system.
- Change the initial value of  $\omega$  until  $\det(\mathbf{C}) = 0$ . This provides the natural (circular) frequency of the system.

It is worth to remark that, especially for higher order natural frequencies, due to the exponential nature of the solution, a lot of care must be paid in determining the zero of the transcendental equation, since they are very close to singular points where the function changes sign, and this hides the zeros. This is a problem also with the path following algorithm, since it requires using very small increments of the driving parameters, well below the needed accuracy, which increase the CPU time.

#### 4.1. The simplified problem

As previously said, in this case the natural frequencies practically depend on the two parameters  $\delta_1$  and  $\delta_2$  only. The first two frequencies are reported in Fig. 4, where we see that the  $\omega$ s are increasing functions of  $\delta_1$  and decreasing functions of  $\delta_2$ . In the particular case  $\delta_1 = \delta_2$  (which has only a mathematical interest since it corresponds to the unrealistic case  $h=0$ , see (13)) the frequencies are solutions of  $\cosh(\delta_3^{1/4} \omega^{1/2}) \cos(\delta_3^{1/4} \omega^{1/2}) = 1$  and thus are independent of  $\delta_1$  and  $\delta_2$ ; the first four are  $\omega_{1,\text{lim}} = 22.373/\sqrt{\delta_3}$ ,  $\omega_{2,\text{lim}} = 61.673/\sqrt{\delta_3}$  (see the dashed lines in Fig. 4),  $\omega_{3,\text{lim}} = 120.903/\sqrt{\delta_3}$  and  $\omega_{4,\text{lim}} = 199.859/\sqrt{\delta_3}$ .

In the following we will see how the natural frequencies of the general problem approach the values of Fig. 4 when  $\varrho_1 \rightarrow 0$ ,  $\varrho_2 \rightarrow 0$ ,  $\eta_1 \rightarrow \infty$ ,  $\eta_2 \rightarrow \infty$ ,  $\zeta_1 \rightarrow 0$ ,  $\zeta_2 \rightarrow 0$  and  $k_N \rightarrow \infty$ .

#### 4.2. The general case

##### 4.2.1. Example 1

For the parameters we are not interested to vary we consider  $\mu_1 = 15$ ,  $\mu_2 = 16$ ,  $h_1 = 0.04$ ,  $h_2 = 0.05$ ,  $k_T = 10$ , which provide  $\delta_1 = 1.33024$ ,  $\delta_2 = 1.29167$ , so that  $\omega_{1,\text{lim}} = 22.410979/\sqrt{\delta_3}$ ,  $\omega_{2,\text{lim}} = 61.700960/\sqrt{\delta_3}$ ,  $\omega_{3,\text{lim}} = 120.932248/\sqrt{\delta_3}$ , etc. (see Section 4.1). We further assume  $\alpha = 1.1$ ,  $\beta = 1.15$ , which yields  $\delta_3 = 1.02381$  and

$$\begin{aligned}\omega_{1,\text{lim}} &= 22.1488, \\ \omega_{2,\text{lim}} &= 60.9793, \\ \omega_{3,\text{lim}} &= 119.5178.\end{aligned}\tag{22}$$

To study the convergence of the natural frequencies toward those of the simplified problem we consider  $\varrho_1 = 10^{-q}$ ,  $\varrho_2 = 10^{-q}$ ,  $\eta_1 = 10^q$ ,  $\eta_2 = 10^q$ ,  $\zeta_1 = 10^{-q}$ ,  $\zeta_2 = 10^{-q}$  and  $k_N = 10^q$  and compute the frequencies for increasing values of  $q$ . Their are reported in Fig. 5, which is obtained by a self-made adaptive path following algorithm.



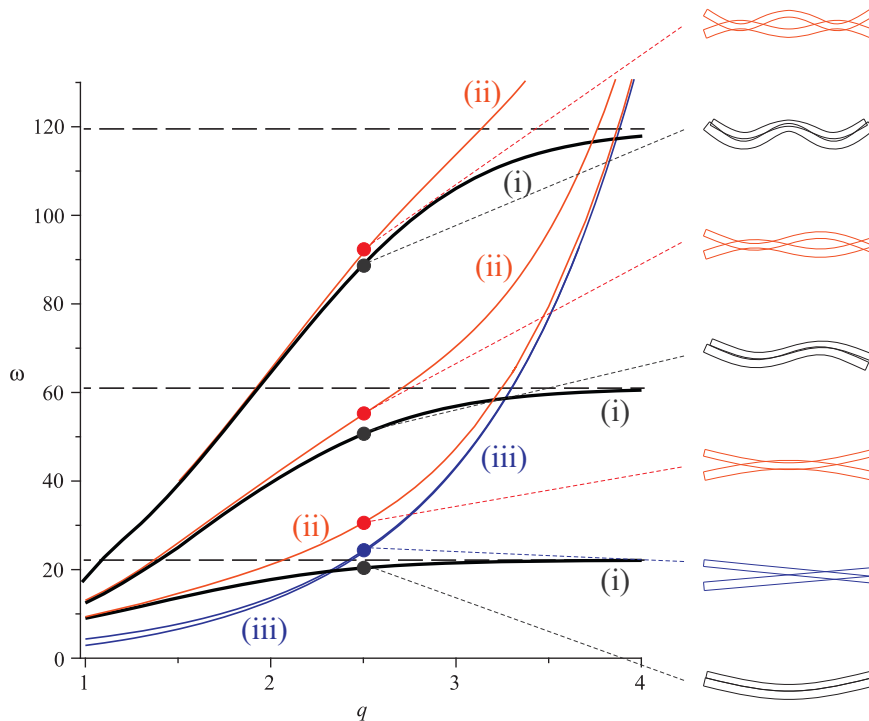


**Fig. 5.** The main natural frequencies for  $\mu_1 = 15$ ,  $\mu_2 = 16$ ,  $h_1 = 0.04$ ,  $h_2 = 0.05$ ,  $k_T = 10$ ,  $\alpha = 1.1$ ,  $\beta = 1.15$ ,  $q_i = 10^{-q}$ ,  $\eta_i = 10^q$ ,  $\zeta_i = 10^{-q}$  and  $k_N = 10^q$ . The normal modes for  $q=2.5$  are, from below to above: first 'classical' mode,  $\omega = 20.3707$ ; rigid rotation mode,  $\omega = 23.8863$ ; first anti-phase mode,  $\omega = 30.5538$ ; second 'classical' mode,  $\omega = 50.6103$ ; second anti-phase mode,  $\omega = 55.0665$ ; third 'classical' mode,  $\omega = 88.8953$ ; third anti-phase mode,  $\omega = 91.4324$ . The mode shapes are out of scale (in particular, they are enlarged in the transversal direction) for a better visual understanding. (For interpretation of the references to colour in this figure caption, the reader is referred to the web version of this article.)

We can distinguish different families of curves (colours in the online version):

1. the thick black lines (marked with (i) in Fig. 5) correspond to the 'classical' (in-phase) first, second and third modes;
2. the dashed lines correspond to the asymptotic values (22);
3. the red curves (marked with (ii) in Fig. 5) correspond to anti-phase first, second and third modes. It is worth to remark that for low values of  $q$  the two layers are practically disjoint (in the normal direction), so that it is not surprising that red and black curves coincide in the left part of the diagram;
4. the blue lines (marked with (iii) in Fig. 5) correspond to rigid bodies modes, one where the layers rotate in anti-phase (to be precise, this is not exactly a rigid mode, since the layers have an infinitesimal curvature) and the other where the layers undergo an anti-phase vertical translation (this is instead exactly a rigid mode). For the latter case the natural frequency can be computed easily, and is given by  $\omega_{rm} = \sqrt{k_N(1+\beta)/\beta}$ .

The main conclusion that can be drawn from Fig. 5 is that the natural frequencies associated to 'classical' mode converge for  $q \rightarrow \infty$  to the values prescribed by the simplified problem, while the natural frequencies of the anti-phase modes first converge to those of the rigid modes, and then together diverge toward infinity. The first point confirms expectation, while the second point agrees very well with the fact that anti-phase and rigid modes are not present in the simplified case, since they involve an incompatible kinematics (more precisely, they are incompatible with the hypothesis of interface perfect adherence in the normal direction).

To have a better feeling on the rate of convergence of 'classical' modes, and also to quantitatively judge on the achievement the limit values, we report in Fig. 6 the ratios  $\omega_i(q)/\omega_{i,\text{lim}}$ . Clearly, the higher is the mode, the slower is the convergence. More precisely, we see that  $\omega_2(q)/\omega_{2,\text{lim}}$  is shifted of about  $\Delta q = 0.4$  with respect to  $\omega_1(q)/\omega_{1,\text{lim}}$ , while  $\omega_3(q)/\omega_{3,\text{lim}}$  is shifted of about  $\Delta q = 0.3$  with respect to  $\omega_2(q)/\omega_{2,\text{lim}}$ . This means that the convergence of  $\omega_1(q)$  is  $10^{0.4} \simeq 2.5$  times faster than that of  $\omega_2(q)$ , whose convergence is instead  $10^{0.3} \simeq 2$  times faster than that of  $\omega_3(q)$ .

Once the acceptable error in the frequencies has been established, Fig. 6 permits us to determine the threshold value of  $q$  above which the simplified problem provides adequate results. For example, if the error should be lesser than 2 percent,  $q$  must be greater than 3.155 for the first mode, greater than 3.56 for the second mode and greater than 3.835 for the third mode. These are examples of a quantitative measure of when the axial and rotational inertia can be neglected, of when the

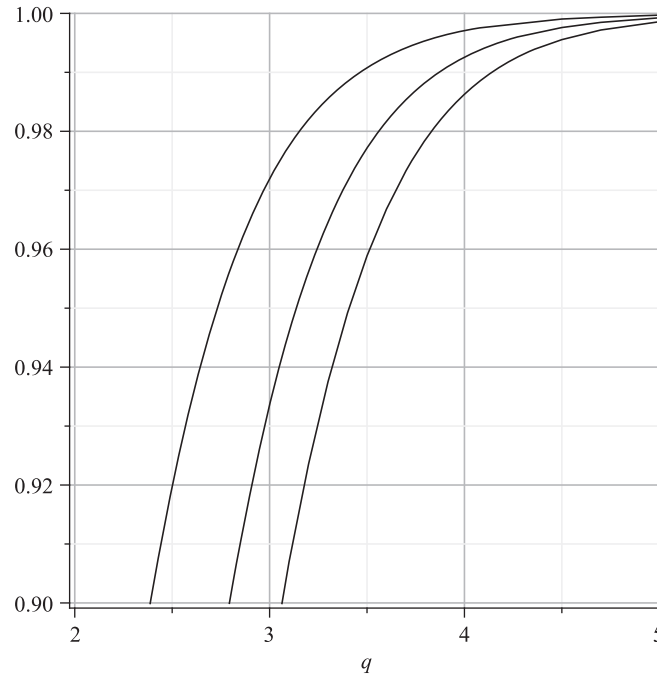


Fig. 6. The ratios  $\omega_i(q)/\omega_{i,\text{lim}}$  for the first three modes. Parameters as in Fig. 5.

shear deformations are negligible, and of when the layers can be considered in perfect contact in the normal direction; they improve vague sentences usually reported in the literature, which generically say “when the beams are slender enough”.

The previous one is an exact criterion. In addition to this, Fig. 5 suggests in this case an approximate criterion to established the achievement of the limit value, i.e., the validity of the simplified model. In fact, we see that when the blue curve  $\omega_{rm}$  intersects the dashed paths, the error is small (actually, it is around 5 percent) and likely it is acceptable from a practical point of view. We can then conclude that the frequency  $\omega_i$ , computed by the simplified model, is reliable for

$$q > \log_{10} \left( \frac{\omega_i^2 \beta}{1 + \beta} \right). \quad (23)$$

#### 4.2.2. Example 2

To extend the previous analysis, and to enlarge its overall meaning, in this subsection we consider the steel–concrete beam investigated experimentally and numerically by Dilella and Morassi [8,27]. More precisely, we consider the beam denoted as “T1PR” in [8]. For that two-layer beam we have  $L=3.5$  m;  $E_1=4.2863 \times 10^{10}$  N/m<sup>2</sup>,  $\nu_1=0.166$ ,  $G_1=E_1/(2(1+\nu_1))=1.8380 \times 10^{10}$  N/m<sup>2</sup>,  $\rho_1=2440$  kg/m<sup>3</sup> (concrete);  $A_1=3.00 \times 10^{-2}$  m<sup>2</sup>,  $J_1=9.00 \times 10^{-6}$  m<sup>4</sup>,  $h_1=0.03$  m,  $\chi_1=1.2$  (slab);  $E_2=21 \times 10^{10}$  N/m<sup>2</sup>,  $\nu_2=0.3$ ,  $G_2=E_2/(2(1+\nu_2))=8.0769 \times 10^{10}$  N/m<sup>2</sup>,  $\rho_2=7866$  kg/m<sup>3</sup> (steel);  $A_2=0.164 \times 10^{-2}$  m<sup>2</sup>,  $J_2=5.41 \times 10^{-6}$  m<sup>4</sup>,  $h_2=0.07$  m,  $\chi_2=2.49$  (beam);  $\hat{k}_T=1.216 \times 10^9$  N/m<sup>2</sup>,  $\hat{k}_N=2.749 \times 10^9$  N/m<sup>2</sup> (identified interface stiffnesses). We refer to [8] for more details.

The dimensionless parameters associated to the previous physical quantities are  $\varrho_1=1$ ,  $\varrho_2=0.176$ ,  $\eta_1=21012$ ,  $\eta_2=10474$ ,  $\zeta_1=2.45 \times 10^{-5}$ ,  $\zeta_2=4.75 \times 10^{-5}$ ,  $\mu_1=40833$ ,  $\mu_2=10936$ ,  $h_1=0.00857$ ,  $h_2=0.02$ ,  $k_T=4.73 \times 10^5$ ,  $k_N=10.7 \times 10^5$ ,  $\alpha=2.945$  and  $\beta=0.176$ . Furthermore, the parameters of the simplified model are  $\delta_1=152.7088$ ,  $\delta_2=54.8378$  and  $\delta_3=0.2981$ . With these latter numbers the first eight frequencies of the limit problem are

$$\omega_{1,\text{lim}} = 64.4957,$$

$$\omega_{2,\text{lim}} = 159.6561,$$

$$\omega_{3,\text{lim}} = 286.0624,$$

$$\omega_{4,\text{lim}} = 442.1566,$$

$$\omega_{5,\text{lim}} = 630.2348,$$

$$\omega_{6,\text{lim}} = 851.6580,$$

$$\omega_{7,\text{lim}} = 1107.6105,$$

$$\omega_{8,\text{lim}} = 1398.6241. \quad (24)$$

Similar to the previous example, to study the convergence of the natural frequencies toward those of the simplified problem we consider  $\varrho_1 = 1 \times 10^{-q}$ ,  $\varrho_2 = 0.176 \times 10^{-q}$ ,  $\eta_1 = 21012 \times 10^q$ ,  $\eta_2 = 10474 \times 10^q$ ,  $\zeta_1 = 2.45 \times 10^{-5} \times 10^{-q}$ ,  $\zeta_2 = 4.75 \times 10^{-5} \times 10^{-q}$  and  $k_N = 10.7 \times 10^5 \times 10^q$  and compute the frequencies for increasing values of  $q$ . Note that for  $q=0$  we have Timoshenko beams, while for  $q \rightarrow \infty$  we have Euler–Bernoulli beams. Both cases have been considered in [8]. The first eight frequencies are reported in Fig. 7a, where the asymptotic limits (24) are still drawn with horizontal dashed lines as in Fig. 5.

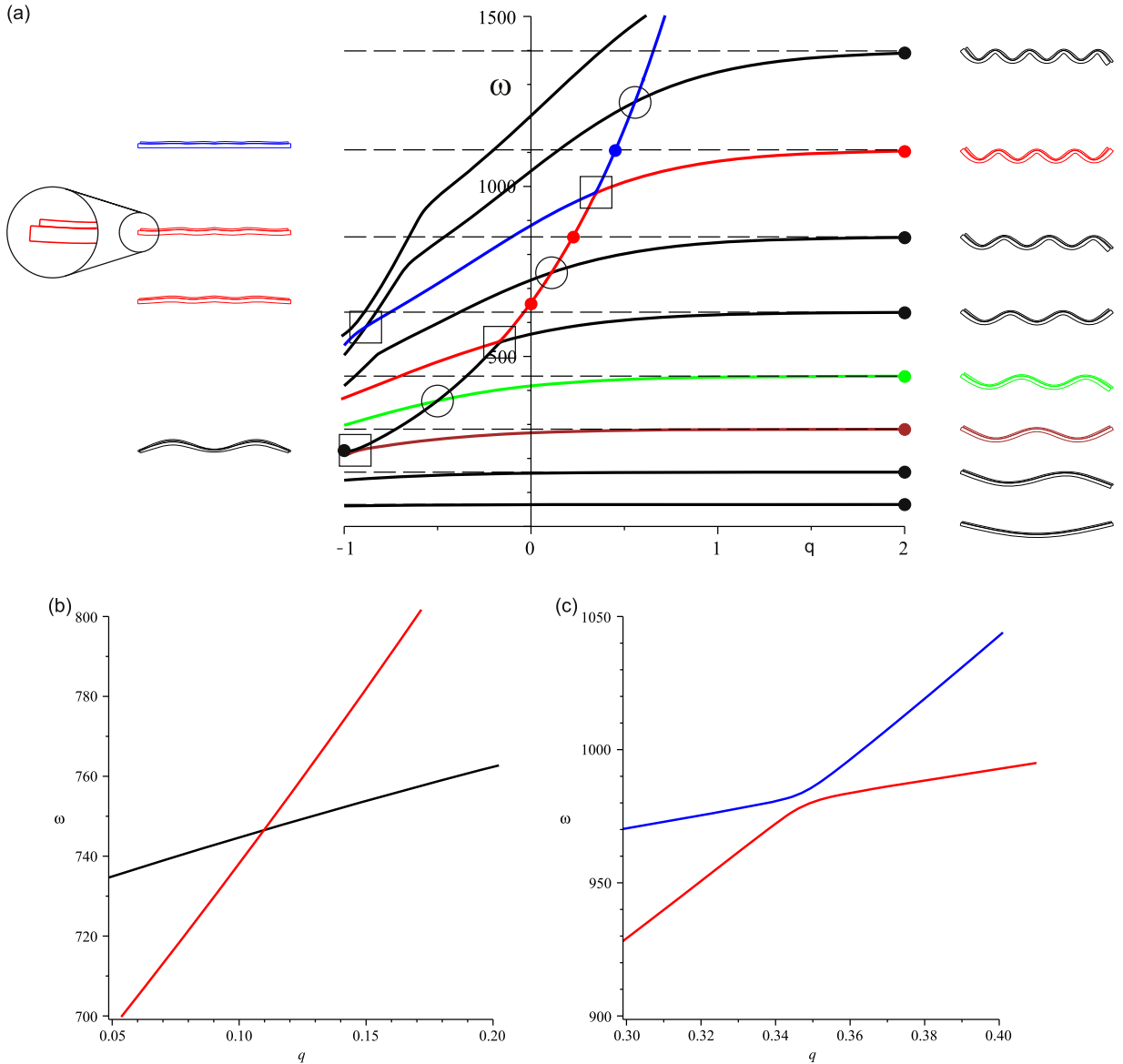


**Fig. 7.** The main natural frequencies for  $\mu_1 = 40833$ ,  $\mu_2 = 10936$ ,  $h_1 = 0.00857$ ,  $h_2 = 0.02$ ,  $k_T = 4.73 \times 10^5$ ,  $\alpha = 2.945$ ,  $\beta = 0.176$ ,  $\varrho_1 = 1 \times 10^{-q}$ ,  $\varrho_2 = 0.176 \times 10^{-q}$ ,  $\eta_1 = 21012 \times 10^q$ ,  $\eta_2 = 10474 \times 10^q$ ,  $\zeta_1 = 2.45 \times 10^{-5} \times 10^{-q}$ ,  $\zeta_2 = 4.75 \times 10^{-5} \times 10^{-q}$  and  $k_N = 10.7 \times 10^5 \times 10^q$ . (a) Large view, (b) zoom of a crossing point and (c) zoom of a veering point. The mode shapes (computed in correspondence of the marked dots) are out of scale (in particular, they are enlarged in the transversal direction) for a better visual understanding. Crossing points are highlighted by surrounding circles, veering points by surrounding squares.

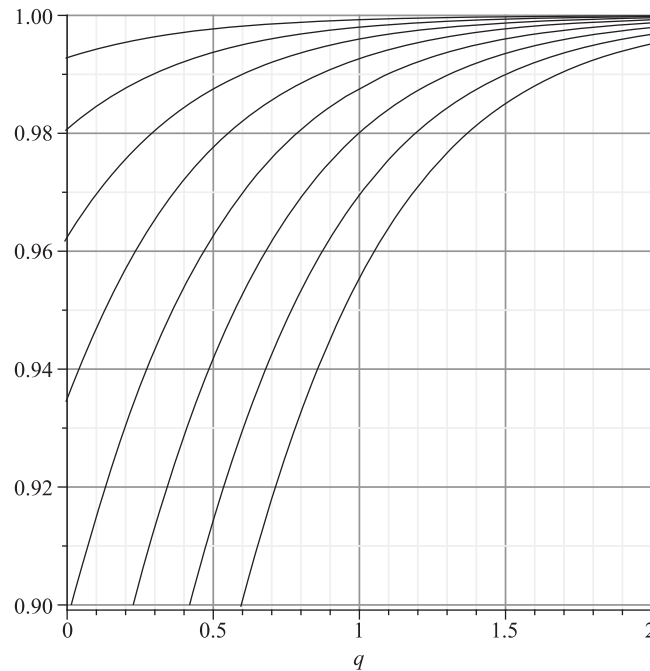


Fig. 8. The ratios  $\omega_i(q)/\omega_{i,\text{lim}}$  for the first eight modes. Parameters as in Fig. 7.

The first observation is that, contrarily to the case of Section 4.2.1, now there are no anti-phase modes. This is a consequence of the fact that even for  $q = -1$  the value of  $k_N$  is yet sufficiently high. The mode shapes of these ‘classical’ (in-phase) modes for  $q = 2$  are reported on the right part of the figure, and clearly show their flexural behaviour.

While for the first three frequencies the convergence toward the limit model is ‘simple’, as in the case of the first three classical modes of Section 4.2.1, for higher modes (not reported in Section 4.2.1) the situation is more involved. In particular, we have that all paths ‘intersect’ an almost parabolic path. Four mode shapes along this path (in correspondence of the four marked dots) are reported on the left part of the figure and show that this is a mode where mainly slipping axial vibrations are involved (see the enlargement on the left), similarly to what happens in the path (\*) of the forthcoming Fig. 11. Thus, this nonflexural path is mainly dominated by the axial stiffnesses and by the tangential interface stiffness. In particular, the larger is  $k_T$  the more this path shifts toward the left.

In the range  $q \in [0, 2]$ , i.e., in between the Timoshenko and the Euler–Bernoulli beams, the ‘intersection’ involves only the modes higher than the sixth, and so cannot be appreciated with lower modes. However, seventh modes can be detected experimentally, see [8].

The ‘intersection’ between the ‘classical’ and the nonflexural modes are of two types: we have both crossing and veering. An example of the former is reported in Fig. 7b, while an example of the latter is reported in Fig. 7c. In the overall picture of Fig. 7a the crossing points are highlighted by surrounding circles, while veering points by surrounding squares. It is worth to note that they alternate on the parabolic-like path.

The previous results show how complicated the overall frequencies scenario for varying parameters is. This aspect is further (and better) highlighted in the next Section 4.3.

To determine the rate of convergence also in this case, we report in Fig. 8 (which is the counterpart of Fig. 6 of Section 4.2.1) the ratios  $\omega_i(q)/\omega_{i,\text{lim}}$ . Again, as expected, the higher is the mode, the slower is the convergence.

As Fig. 6 did, also Fig. 8 allows us to determine the threshold value of  $q$  above which the simplified problem provides adequate results. For example, if we still keep the error threshold at 2 percent,  $q$  must be greater than 0 for the second mode (i.e., the Timoshenko beam is enough), greater than 0.293 for the third mode, greater than 0.553 for the fourth mode, greater than 0.842 for the fifth mode, greater than 1.027 for the sixth mode, greater than 1.235 for the seventh mode and greater than 1.386 for the eighth mode.

#### 4.3. The effects of the various parameters

In Section 4.2 the seven parameters of interest  $q_i$ ,  $\eta_i$ ,  $\zeta_i$  and  $k_N$  have been varied simultaneously toward their limit values. This permits us to understand the overall picture, and to assess the rate of convergence, but does not provide any information on the effect of each parameter on the convergence. For example, it has not been shown that if one parameter is more important than the other with respect to the closeness to the simplified problem (and thus with respect to the reliability of

this latter). It also gives the practical thresholds for each parameter. This issue is considered in this subsection, where we vary independently the relevant parameters, while always keeping fixed  $\mu_1 = 15$ ,  $\mu_2 = 16$ ,  $h_1 = 0.04$ ,  $h_2 = 0.05$ ,  $k_T = 10$ ,  $\alpha = 1.1$  and  $\beta = 1.15$  as in Section 4.2.1. Due to the lack of space, we do not report the same analysis for the case of Section 4.2.2.

As an initial reference case we consider  $\varrho_1 = 0.2$ ,  $\varrho_2 = 0.3$ ,  $\eta_1 = 10$ ,  $\eta_2 = 14$ ,  $\zeta_1 = 0.1$ ,  $\zeta_2 = 0.11$ . The parameter  $k_N$ , on the other hand, is used as a driving parameter.

The first 10 frequencies as a function of  $k_N$  are reported in Fig. 9, where we clearly distinguish two families of natural frequencies: those which are almost independent of  $k_N$ , which are reported in black and numbered with even numbers, and those which vary by increasing  $k_N$ , which are reported in red and numbered with odd numbers (colours in the online version). Black and red paths are monotonic and intersect in single crossover points, where internal resonance phenomena occur. This happens only for ‘medium’ values of  $k_N$  (in between 200 and 2000), since for small and large values of  $k_N$  the paths keep well disjoint (apart from (2) and (3) which coalesce for  $k_N \rightarrow 0$ , a fact that it is not surprising since they correspond to the first in-phase and first in anti-phase modes, respectively, see Fig. 9).

The different dependence on  $k_N$  reflects a different nature of the associated vibrating modes, which are also reported in Fig. 9 for  $k_N = 10$  (‘low’ value) and for  $k_N = 10^5$  (‘high’ value). These modes are normalised by assuming that the dimensionless strain energy, given by

$$2\mathcal{E} = \int_0^1 [(\Theta'_1)^2 + \alpha(\Theta'_2)^2 + \mu_1(W'_1)^2 + \mu_2(W'_2)^2 + \eta_1(V'_1 + \Theta_1)^2 + \eta_2(V'_2 + \Theta_2)^2 + k_N S_N^2 + k_T S_T^2] dz, \quad (25)$$

is equal in all modes.

For low values of  $k_N$ , apart from the first black mode (2), the interface detachment in the normal direction is clearly visible in all modes, including the rigid body (1) and the first anti-phase mode (3). Note that modes higher than the third are characterised by a bending deformation involving mainly one layer. The first red curve (1) corresponds to a rigid rotation, and accordingly goes to 0 for  $k_N \rightarrow 0$  since in this case there is no stiffness in that mode.

It is for high values of  $k_N$  (where there is no longer detachment in the normal direction, although slip occurs, see e.g., path (4)) that the difference between black and red modes is more evident. In fact, while black modes corresponds

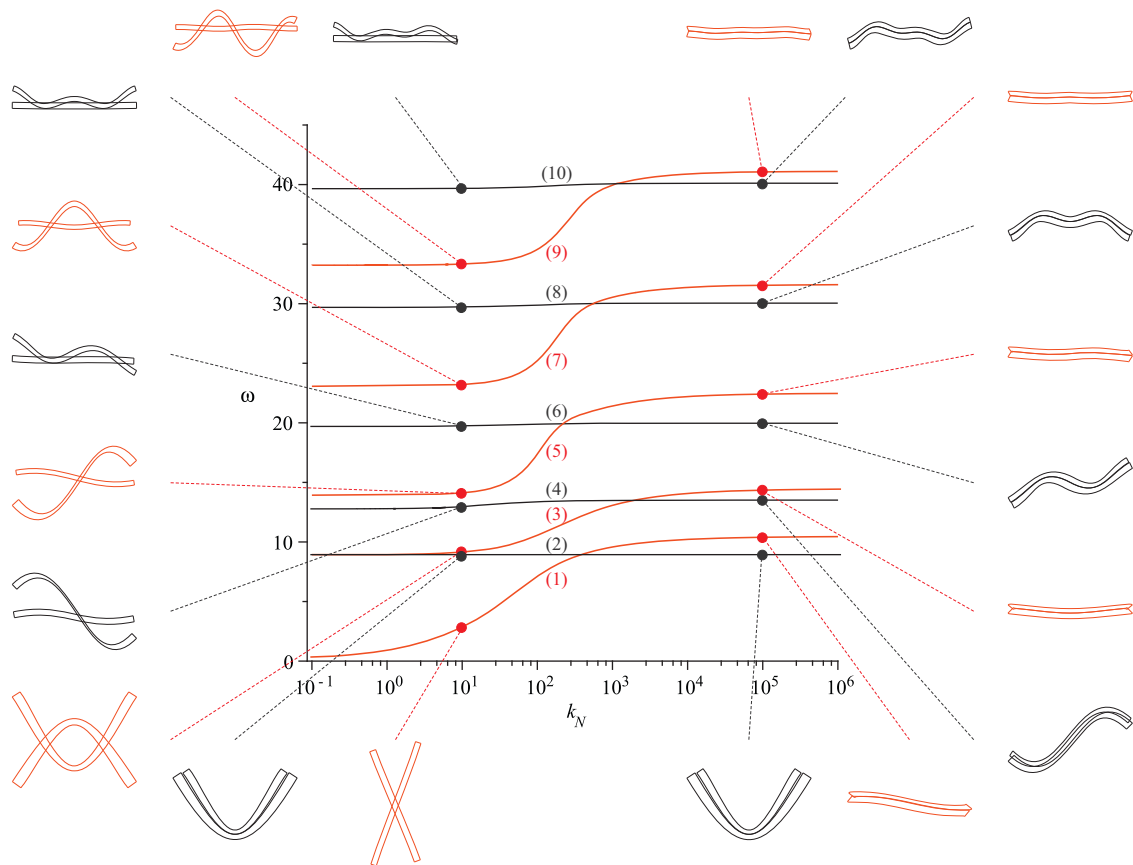


**Fig. 9.** The first 10 frequencies as a function of  $k_N$  and some associated normal modes.  $\mu_1 = 15$ ,  $\mu_2 = 16$ ,  $h_1 = 0.04$ ,  $h_2 = 0.05$ ,  $k_T = 10$ ,  $\alpha = 1.1$ ,  $\beta = 1.15$ ,  $\varrho_1 = 0.2$ ,  $\varrho_2 = 0.3$ ,  $\eta_1 = 10$ ,  $\eta_2 = 14$ ,  $\zeta_1 = 0.1$  and  $\zeta_2 = 0.11$ . The mode shapes are out of scale (in particular, they are enlarged in the transversal direction) for a better visual understanding. (For interpretation of the references to colour in this figure caption, the reader is referred to the web version of this article.)

to ‘classical’ flexural modes, where now both layers oscillate jointly, the red one corresponds to ‘uncommon’ modes characterised by marked shear oscillations with apparently minor flexural content.

To have a better understanding on the normal mode characteristics, their energy contents are reported in Table 1. The ‘classical’ black paths (2)–(6)–(8)–(10) are mainly flexural and practically independent of  $k_N$ . Only the black path (4) has a different behaviour with energy that concentrates on shear deformations. The energy at the interface is always negligible.

‘Uncommon’ red paths, on the other hand, have a more complicated behaviour, with a remarkable flux of energy from one component to the others. For increasing  $k_N$ , in path (1) the energy flows from interface to shear, with a negligible flexural content. In path (3) the energy flows from flexure to shear, although in the limit case bending is still important. In paths (5)–(7)–(9) energy flows from shear to flexure. In the latter four cases, the interface energy has a maximum for about  $k_N = 10^2$ , showing how the transition from low to high values of  $k_N$  involves interface.

Another property suggested by Table 1 is that around cross-over points, energy is mainly flexural. This can be noted in paths (5)–(7)–(9), which have a maximum of the flexural energy around  $k_N = 10^3$ , i.e., just close to the cross-over points which are  $k_N = 10^{2.338}$ ,  $k_N = 10^{2.752}$  and  $k_N = 10^{3.053}$ , respectively.

As far as the spatial distribution of energy is concerned, we note that in red paths the total strain energy is localised at the boundaries for low values of  $k_N$  while it is almost uniformly distributed along the beam for high values of  $k_N$ , as shown in Fig. 10.

**Table 1**

Energies on paths of Fig. 9. In bold the dominant one, which characterise the mode.

Path #	$k_N$	$\omega$	$\frac{\mathcal{E}_{\text{flexural}}}{\mathcal{E}_{\text{total}}} (\%)$	$\frac{\mathcal{E}_{\text{axial}}}{\mathcal{E}_{\text{total}}} (\%)$	$\frac{\mathcal{E}_{\text{shear}}}{\mathcal{E}_{\text{total}}} (\%)$	$\frac{\mathcal{E}_{\text{interface}}}{\mathcal{E}_{\text{total}}} (\%)$
(1)	$10^1$	2.8546	0.23	0.00	5.16	<b>94.61</b>
(1)	$10^2$	7.1143	2.09	0.00	45.59	<b>52.32</b>
(1)	$10^3$	9.5771	1.40	0.00	<b>88.17</b>	10.43
(1)	$10^4$	10.2131	0.32	0.00	<b>96.99</b>	2.69
(1)	$10^5$	10.3931	0.20	0.00	<b>98.99</b>	0.80
(2)	$10^1$	8.9356	<b>95.62</b>	0.05	4.05	0.28
(2)	$10^3$	8.9357	<b>95.62</b>	0.05	4.04	0.28
(2)	$10^5$	8.9359	<b>95.63</b>	0.05	4.04	0.28
(3)	$10^1$	9.1493	<b>92.79</b>	0.00	2.44	4.77
(3)	$10^2$	10.5513	<b>77.62</b>	0.00	1.42	20.95
(3)	$10^3$	13.0719	<b>57.46</b>	0.00	30.97	11.57
(3)	$10^4$	14.0700	<b>49.79</b>	0.00	47.16	3.04
(3)	$10^5$	14.3506	47.78	0.00	<b>51.36</b>	0.86
(4)	$10^1$	12.9627	14.81	0.00	<b>82.48</b>	2.71
(4)	$10^3$	13.4801	19.29	0.00	<b>80.14</b>	0.57
(4)	$10^5$	13.5109	19.16	0.00	<b>80.52</b>	0.32
(5)	$10^1$	14.1179	23.41	0.00	<b>73.28</b>	3.31
(5)	$10^2$	17.3607	32.09	0.00	25.97	<b>41.94</b>
(5)	$10^3$	21.4129	<b>84.37</b>	0.00	10.03	5.60
(5)	$10^4$	22.2041	<b>79.80</b>	0.00	18.73	1.47
(5)	$10^5$	22.4098	<b>78.38</b>	0.00	21.24	0.38
(6)	$10^1$	19.7371	<b>78.93</b>	0.00	20.64	0.43
(6)	$10^3$	19.9582	<b>75.78</b>	0.00	24.06	0.15
(6)	$10^5$	19.9663	<b>75.56</b>	0.00	24.36	0.08
(7)	$10^1$	23.2095	25.50	0.34	<b>72.81</b>	1.34
(7)	$10^2$	25.2352	29.72	0.00	<b>50.46</b>	19.82
(7)	$10^3$	30.5387	<b>92.47</b>	0.00	2.96	4.57
(7)	$10^4$	31.3696	<b>89.92</b>	0.00	9.10	0.98
(7)	$10^5$	31.5527	<b>88.94</b>	0.00	10.83	0.22
(8)	$10^1$	29.7213	<b>80.56</b>	0.00	19.23	0.21
(8)	$10^3$	30.0261	<b>78.22</b>	0.01	21.59	0.18
(8)	$10^5$	30.0468	<b>77.75</b>	0.01	22.21	0.04
(9)	$10^1$	33.3285	28.21	0.00	<b>71.16</b>	0.62
(9)	$10^2$	34.5567	31.80	0.00	<b>58.97</b>	9.23
(9)	$10^3$	39.9092	<b>95.15</b>	0.00	0.46	4.40
(9)	$10^4$	40.8841	<b>93.93</b>	0.00	5.28	0.78
(9)	$10^5$	41.0647	<b>93.24</b>	0.00	6.60	0.15
(10)	$10^1$	39.6779	<b>81.05</b>	0.00	18.83	0.12
(10)	$10^3$	40.0793	<b>77.95</b>	0.00	21.57	0.48
(10)	$10^5$	40.1124	<b>77.91</b>	0.00	22.07	0.02

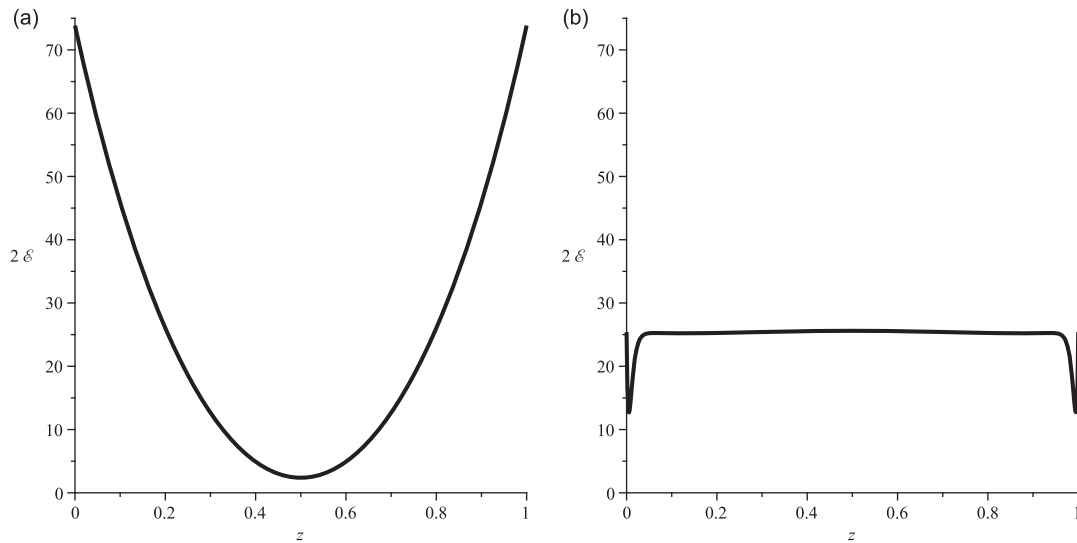


Fig. 10. The strain energy  $\mathcal{E}(z)$  for (a)  $k_N = 10^1$  and (b)  $k_N = 10^6$  on the red path (1) of Fig. 9.

The main conclusion that can be drawn from the previous considerations is that  $k_N$  affects sensibly the ‘uncommon’ modes, much less the ‘classical’ ones, at least in the considered range.

Fig. 9 (and partially Table 1) shows that for  $k_N \simeq 10^5$  the asymptotic values are reached, so that this can be considered as a practical threshold for layer perfect adherence in the normal direction. However, the asymptotic limits are different from those obtained by the simplified problem (Eq. (22)), and this shows that the other parameters are far from their negligibility thresholds.

**Remark 1.** Table 1 shows that the axial strain is always negligible. This suggests that in this case axial inertia is also negligible. Actually, to support this observation, in not reported numerical simulations we have assumed  $\varrho_1 = \varrho_2 = 1$  and  $\varrho_1 = \varrho_2 = 0.001$  and we have obtained practically the same curves of Fig. 9, with negligible numerical differences. This confirms that axial inertia is negligible, at least in this range of parameters.

Shear deformations are not small for large values of  $k_N$ . This implies that the shear stiffnesses  $\eta_1 = 10$  and  $\eta_2 = 14$  are not large enough, and likely that the rotational inertias  $\zeta_1 = 0.1$  and  $\zeta_2 = 0.11$  are not small enough. Furthermore, this shows why the natural frequencies for large  $k_N$  are far from those of the simplified problem (e.g., 8.9359 vs 22.1488 for the first bending mode), since in the simplified problem the kinematics is not rich enough to describe shear deformations.

The subsequent parameters to be increased are then the shear stiffnesses  $\eta_i$ . In Fig. 11 we have fixed  $k_N = 10^5$  and  $\eta_2 = 1.4\eta_1$ , and we increase  $\eta_1$  from 10 (so that the initial point of each curve is on the corresponding curve of Fig. 9) to  $10^3$ . From this figure we see that the first mode is practically independent of  $\eta_1$  and  $\eta_2$ , since  $\omega_1(\eta_1 = 10) = 8.9359$  while  $\omega_1(\eta_1 = 10^5) = 9.0940$ , the difference being of 1.8 percent only.

The higher modes have a different behaviour. All have an initial increasing path, meaning that the stiffening of the system has important effects in this range. There are several veering points, where the paths get closer, without intersecting, and then run away, and also crossing points. Examples of how complicated is the paths behaviour are reported in Fig. 11b, which shows a veering point crossed by two intersection points of another path, and in Fig. 11c.

After the last veering point, each path suddenly approaches its asymptotic limit, which corresponds to ‘classical’ flexural mode shapes, as shown by the normal modes reported on the right side of Fig. 11a and as confirmed by Table 2, which guarantees that for  $\eta_1 = 10^3$  the bending energy is more than 99 percent.

One transition from ‘uncommon’ to ‘classical’ modes through the veering points is illustrated on the path (1) of Fig. 11a and in Table 2, which shows how the energy flows from shear to flexure. The expected conclusion is that increasing the shear stiffness eliminates the ‘strange’ modes involving shear oscillations.

Concerning the  $\eta_1$  limit threshold, above which shear stiffness is negligible, we note from Fig. 11a that it is mode dependent, since it practically corresponds to the last veering point. For example, for the first mode  $\eta_1 = 10$  is enough, while for the second mode  $\eta_{1,cr} \simeq 30$  and for the third mode  $\eta_{1,cr} \simeq 100$  (see Fig. 11b).

In Fig. 11a it is noticeable the presence of a new path, denoted by (\*) and reported in blue. It starts from an axial mode (and this is why it is not reported in Fig. 9), as shown by its initial mode shape, which is similar to the nonflexural mode of Fig. 7. Then after various veering points it becomes shear, flexural, again axial and finally flexural, as shown in Table 2. The detail detection of each veering point, as well as the detection of other axial modes, is out of the scopes of the present

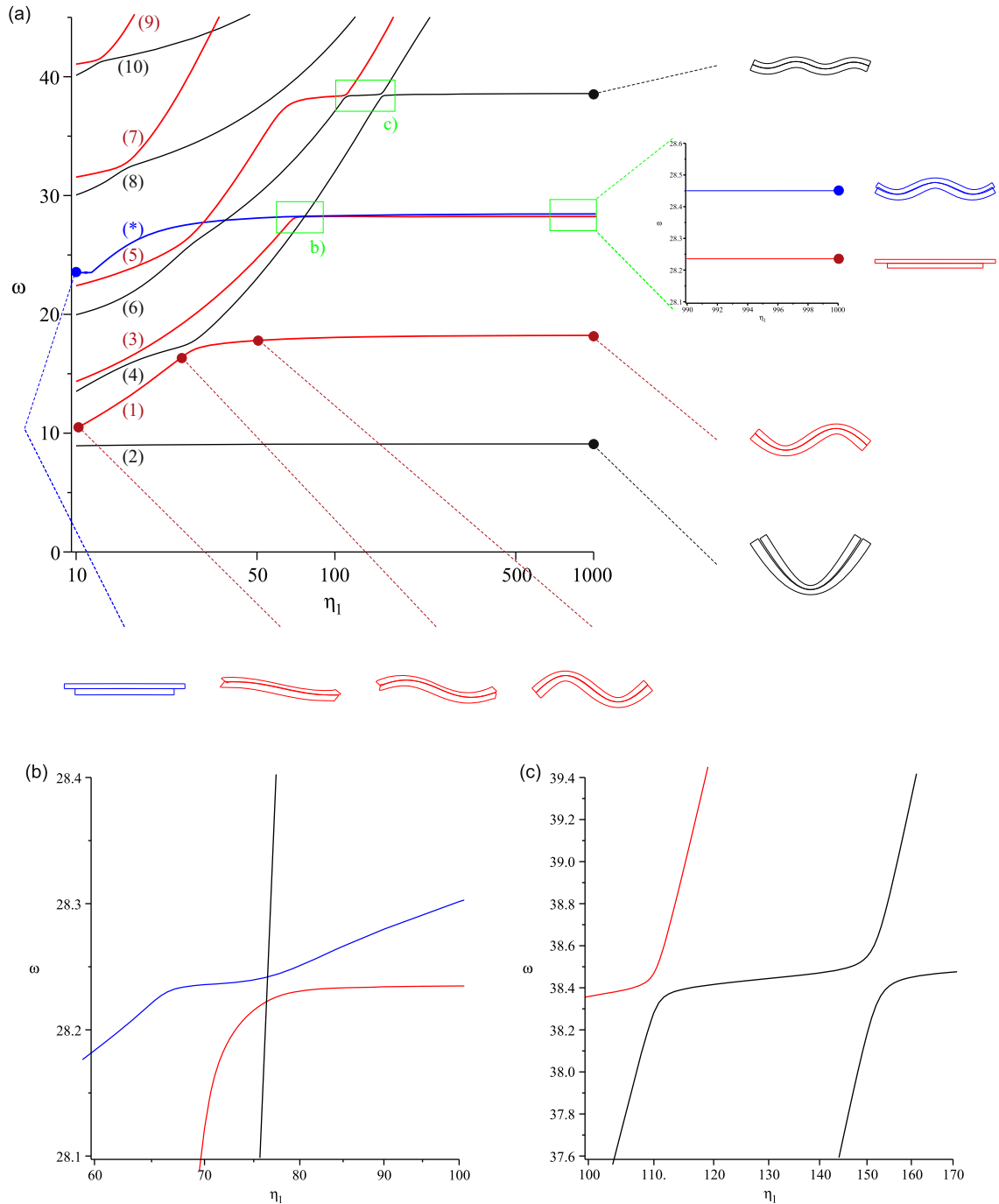


**Fig. 11.** Natural frequencies as a function of  $\eta_1$  for  $\mu_1 = 15$ ,  $\mu_2 = 16$ ,  $h_1 = 0.04$ ,  $h_2 = 0.05$ ,  $k_T = 10$ ,  $\alpha = 1.1$ ,  $\beta = 1.15$ ,  $q_1 = 0.2$ ,  $q_2 = 0.3$ ,  $k_N = 10^5$ ,  $\eta_2 = 1.4\eta_1$ ,  $\zeta_1 = 0.1$  and  $\zeta_2 = 0.11$ . (a) Large view (the numbers of the paths are the same as in Fig. 9) and (b) and (c) zooms. The mode shapes are out of scale (in particular, they are enlarged in the transversal direction) for a better visual understanding.

paper. We focus only on the last veering point, which is reported in Fig. 11b and which is the most important since here the path (\*) 'exchanges' with path (3) getting the 'classical' third mode and leaving to the path (3) the axial mode, as shown on the right hand side of 11a.

Fig. 11a and the previous considerations clearly show how complex is the natural frequencies scenario for the considered two-layer beam.



**Table 2**  
Energies on some paths of Fig. 11. In bold the dominant one, which characterise the mode.

Path #	$\eta_1$	$\omega$	$\frac{\mathcal{E}_{\text{flexural}}}{\mathcal{E}_{\text{total}}} (\%)$	$\frac{\mathcal{E}_{\text{axial}}}{\mathcal{E}_{\text{total}}} (\%)$	$\frac{\mathcal{E}_{\text{shear}}}{\mathcal{E}_{\text{total}}} (\%)$	$\frac{\mathcal{E}_{\text{interface}}}{\mathcal{E}_{\text{total}}} (\%)$
(2)	$10^3$	9.0926	<b>99.62</b>	0.05	0.03	0.29
(2)	$10^5$	9.0940	<b>99.65</b>	0.05	0.00	0.29
(1)	10	10.3931	0.20	0.00	<b>98.99</b>	0.80
(1)	25	16.2382	11.02	0.00	<b>87.87</b>	1.11
(1)	50	17.7979	<b>93.14</b>	0.00	6.76	0.10
(1)	$10^3$	18.2302	<b>99.71</b>	0.00	0.19	0.10
(1)	$10^5$	18.2471	<b>99.90</b>	0.00	0.00	0.10
(3)	$10^3$	28.2356	0.12	<b>91.97</b>	0.00	7.92
(3)	$10^5$	28.2357	0.10	<b>91.98</b>	0.00	7.92
(*)	10	23.5103	0.01	<b>96.29</b>	0.03	3.66
(*)	12	23.8843	31.11	0.38	<b>68.45</b>	0.06
(*)	20	26.8622	<b>75.70</b>	0.03	24.23	0.04
(*)	60	28.1837	<b>93.16</b>	3.40	3.09	0.35
(*)	70	28.2358	0.09	<b>91.67</b>	0.33	7.91
(*)	80	28.2509	<b>72.71</b>	23.41	1.75	2.13
(*)	90	28.2798	<b>94.55</b>	3.48	1.59	0.37
(*)	120	28.3325	<b>98.16</b>	0.68	1.05	0.11
(*)	$10^3$	28.4504	<b>99.74</b>	0.11	0.10	0.06
(*)	$10^5$	28.4646	<b>99.85</b>	0.09	0.00	0.05
(4)	$10^3$	38.5865	<b>99.89</b>	0.00	0.09	0.02
(4)	$10^5$	38.6028	<b>99.97</b>	0.00	0.00	0.02

Even for very large values of  $\eta_1$  and  $\eta_2$ , where only classical modes survive, we still observe that the natural frequencies are much smaller than those predicted by the simplified model:  $\omega_1 = 9.0940$  ( $\eta_1 = 10^5$ , see Table 2) vs  $\omega_{1,\text{lim}} = 22.1488$  (see (22)),  $\omega_2 = 18.2470$  vs  $\omega_{2,\text{lim}} = 60.9793$  and  $\omega_3 = 38.6029$  vs  $\omega_{3,\text{lim}} = 119.5178$ . This permits to conclude that not only  $k_N \rightarrow \infty$  alone is insufficient, as noted before, but also that  $k_N \rightarrow \infty$  together with  $\eta_1 \rightarrow \infty$  and  $\eta_2 \rightarrow \infty$  are not sufficient to reach the values  $\omega_{i,\text{lim}}$  proposed in (22). Thus, axial and/or rotational inertia are expected to play a major role.

To confirm this fact, we have reported in Fig. 12 the first three frequencies for  $k_N = 10^5$ ,  $\eta_1 = 10^5$ , and  $\eta_2 = 1.4 \times 10^5$ ,  $\varrho_1 = 0.2$ ,  $\varrho_2 = 0.3$ , and for  $\zeta_1 = 0.1p$ ,  $\zeta_2 = 0.11p$ . Note that for  $p=1$  we have the asymptotic limits of Fig. 11 (see Table 2), so that the present analysis continues the previous one.

Fig. 12 shows that in this range the rotational inertia plays a major role, since it is able to change, e.g., the first natural frequency of a factor  $22.1488/9.0940 \simeq 2.5$  (while  $k_N$ ,  $\eta_1$  and  $\eta_2$  are not able to do this).

The curves  $\omega_i(p)$  approach the limit  $p \rightarrow 0$  with a large slope, and the larger is the order of the natural frequency, the larger is the slope. This shows that (i) the simplified problem is very sensitive with respect the rotational inertia (and the sensitivity increases with the order of the frequency) and (ii) that a quantitative critical threshold for  $\zeta_1$  and  $\zeta_2$  is necessarily very small. For example, if we accept an error of about 2.5 percent on  $\omega_1$  with respect to  $\omega_{1,\text{lim}}$ , we have  $\zeta_{1,\text{cr}} \simeq 10^{-3}$  and  $\zeta_2 \simeq 1.1\zeta_{1,\text{cr}}$ .

The enlargements of Fig. 12b, d, and f show that for  $p \rightarrow 0$  the natural frequencies does not approached the limit values (22), as expected since the limits  $p \rightarrow 0$  are obtained with  $\varrho_1 = 0.2$  and  $\varrho_2 = 0.3$  while (22) correspond to  $\varrho_1 = 0$  and  $\varrho_2 = 0$ . However, the differences are so small ( $\omega_{1,p \rightarrow 0} = 22.1304$  vs  $\omega_{1,\text{lim}} = 22.1488$ , error 0.083 percent;  $\omega_{2,p \rightarrow 0} = 60.9752$  vs  $\omega_{2,\text{lim}} = 60.9793$ , error 0.0067 percent;  $\omega_{3,p \rightarrow 0} = 119.4640$  vs  $\omega_{3,\text{lim}} = 119.5178$ , error 0.045 percent) to be certainly negligible from a practical point of view.

**Remark 2.** The previous consideration suggests that, contrarily to the rotational inertia, the axial inertia is not important. To confirm this fact, we have built a curve like that of Fig. 12a but with  $\zeta_1 = 0.1p$ ,  $\zeta_2 = 0.11p$ ,  $\varrho_1 = 0.2p$  and  $\varrho_2 = 0.3p$ , i.e., both rotational and axial inertia masses have been jointly decreased. The differences between this curve and that of Fig. 12a are of the order of 0.1 percent (and this is why we have not reported this curve), proving the negligibility of the axial inertia. This extend to high values of  $\eta_i$  the results previously obtained (see Remark 1) for small values of the shear stiffnesses.

The paths of Fig. 12c and e apparently cross other almost horizontal paths, which are reported in dots in the figures and which are of axial type. Indeed, they are veering points, as shown by the enlargements of Fig. 13, although the paths are so close that the separation can be lost on a large scale. We can then conclude that the convergence toward the limit case  $p \rightarrow 0$  is not 'continuous', although soon after the veering points the main paths recuperate the shape and the energy contents they had before the veering.

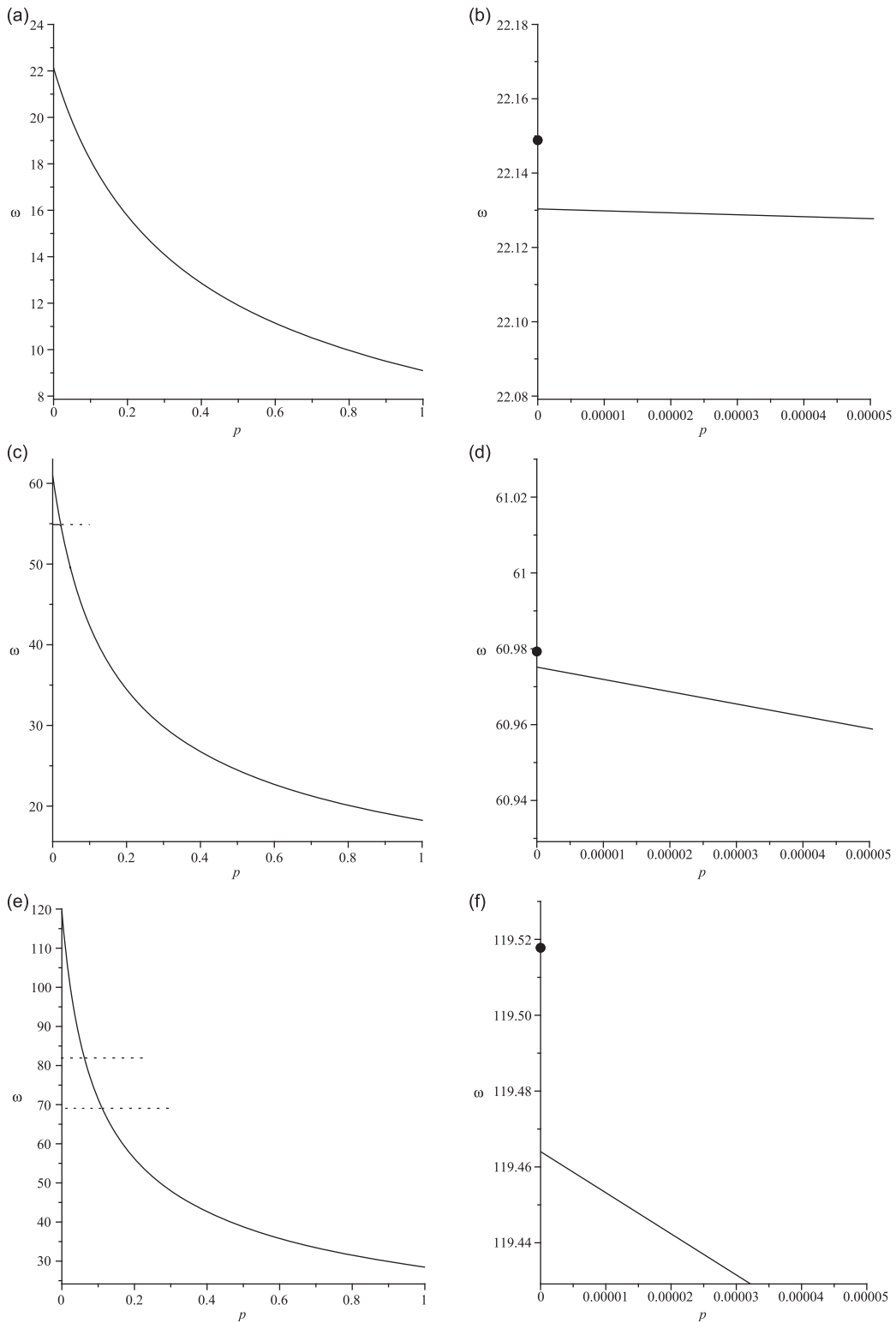


**Fig. 12.** The first three frequencies as a function of  $p$  for  $\zeta_1 = 0.1p$  and  $\zeta_2 = 0.11p$ . The other parameters are  $\mu_1 = 15$ ,  $\mu_2 = 16$ ,  $h_1 = 0.04$ ,  $h_2 = 0.05$ ,  $k_T = 10$ ,  $\alpha = 1.1$ ,  $\beta = 1.15$ ,  $q_1 = 0.2$ ,  $q_2 = 0.3$ ,  $k_N = 10^5$ ,  $\eta_1 = 10^5$ ,  $\eta_2 = 1.4 \times 10^5$ . (a), (c) and (e) normal views and (b), (d) and (f) zooms around  $p=0$ , showing the differences between the present limit  $p \rightarrow 0$  (with  $q_1 = 0.2$  and  $q_2 = 0.3$ ) and the values (22) (obtained with  $q_1 = 0$  and  $q_2 = 0$ , and marked by dots in the figures).

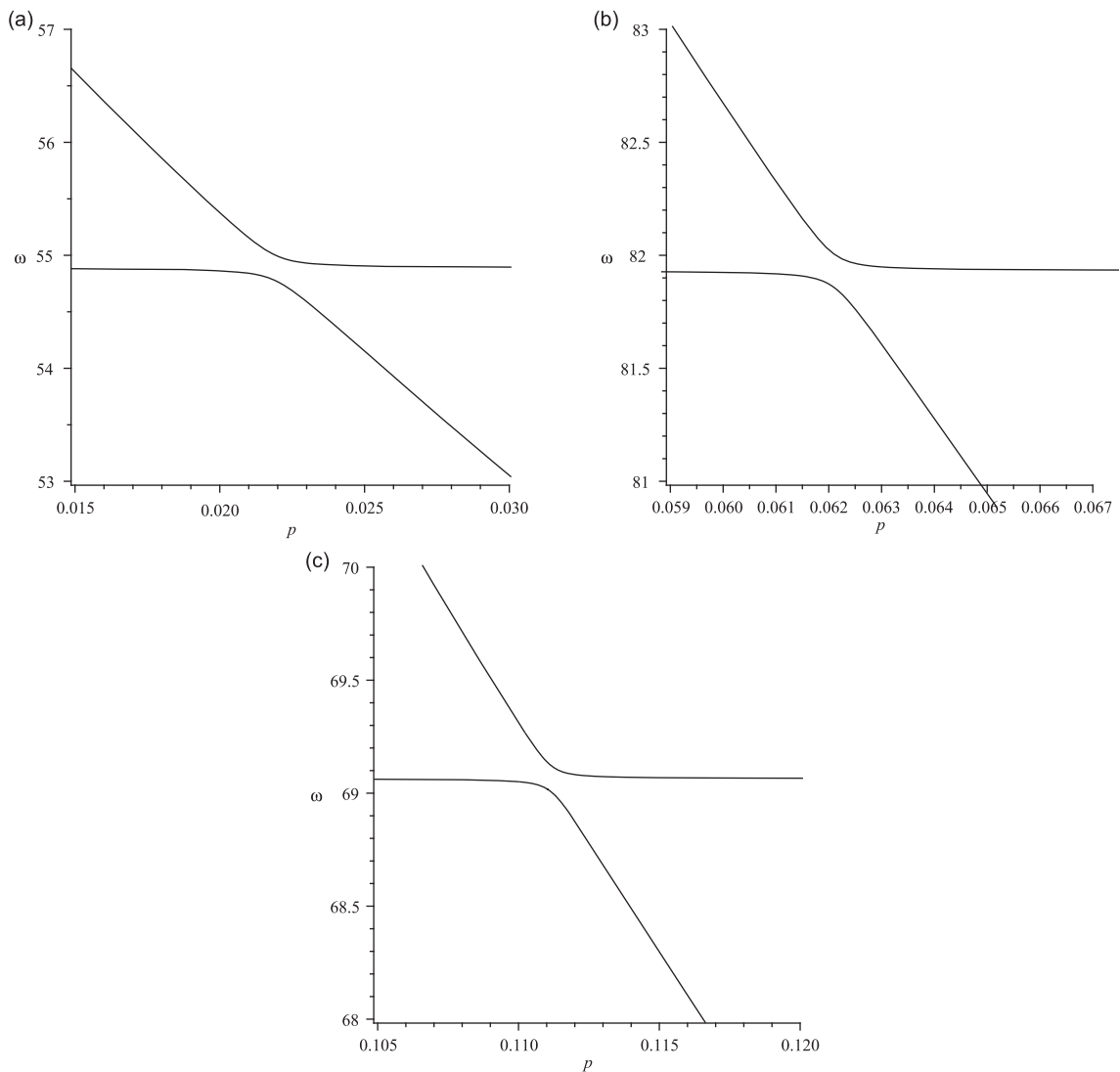


Fig. 13. Enlargements of Fig. 12c and e around the veering points.

## 5. Conclusions

The natural frequencies of a two-layer beam have been investigated in depth with the general aim of assessing the effects of the axial and rotational inertia, of shear stiffness and of interface normal stiffness. Moreover, we have checked when they are negligible, and thus when the simplified model obtained without these contributions is reliable.

First, we have varied jointly the parameters measuring the previous effects, and we have shown the convergence of the ‘classical’ natural frequencies (those associated with ‘classical’ normal modes) of the full problem toward those of the simplified model. We have also identified ‘strange’ normal modes (in particular, anti-phase oscillations of the two beams, slipping and shearing modes); in this case the associated frequencies go to infinity by varying the parameters, according to the fact that they are not present in the limit case. Quantitative estimations of the ratio of convergence have been proposed, and it has been shown that they depend on the order of the natural frequency.

Then, the effects of each parameter have been investigated independently. Somewhat surprisingly, it has been shown that the axial inertia is negligible, contrarily to the rotational inertia which instead plays a role since it affects the natural frequencies considerably, at least in the considered case.

It is shown that some frequencies are almost independent of interface stiffness  $k_N$ , while for the others the transition from limit case  $k_N \rightarrow 0$  to the limit case  $k_N \rightarrow \infty$  is illustrated. When  $k_N \rightarrow \infty$ , a quantitative threshold for the convergence toward the limit values is obtained, and it is shown that it practically does not depend on the frequency order.

The frequency paths for increasing shear stiffnesses  $\eta_i$  have a quite complicated behaviour, involving various crossing and/or veering points. However, after the last veering point, they suddenly approach the asymptotic values obtained for  $\eta_i \rightarrow \infty$ . Above these  $\eta_i$ -thresholds, which strongly depend on the frequency order (contrary to what happens for  $k_N$ ), the layers can be considered as Euler–Bernoulli beams for practical purposes.

Overall, it has been shown that the natural frequencies exhibit a complex behaviour before approaching the values predicted by the simplified model: for example, several veering points, where modes exchanges shapes and energy contents, and some crossing points, where internal resonances occur, have been observed; a region where three paths simultaneously undergo veering and crossing has been identified, too.

## Acknowledgement

This work has been done within the framework of the Centre of Excellence for Modern Composites Applied in Aerospace and Surface Transport Infrastructure—CEMCAST, funded by the European Union under the Seventh Framework Programme, FP7-REGPOT-20091, Grant agreement no. 245479. The financial support is greatly acknowledged.

## References

- [1] R.F. Gibson, A review of recent research on mechanics of multifunctional composite materials and structures, *Composite Structures* 92 (2010) 2793–2810.
- [2] U.A. Girhammar, D. Pan, Dynamic analysis of composite members with interlayer slip, *International Journal of Solids and Structures* 30 (1993) 797–823.
- [3] M.N. Newmark, C.P. Siess, I.M. Viest, Tests and analysis of composite beams with incomplete interaction, *Proceedings of the Society for Experimental Stress Analysis* 9 (1951) 75–92.
- [4] S. Schnabl, M. Saje, G. Turk, I. Planinc, Analytical solution of two-layer beam taking into account interlayer slip and shear deformation, *ASCE Journal of Structural Engineering* 133 (2007) 886–894.
- [5] Q.H. Nguyen, E. Martinelli, M. Hjjaj, Derivation of the exact stiffness matrix for a two-layer Timoshenko beam element with partial interaction, *Engineering Structures* 33 (2011) 298–307.
- [6] C. Adam, R. Heuer, A. Jeschko, Flexural vibrations of elastic composite beams with interlayer slip, *Acta Mechanica* 125 (1997) 17–30.
- [7] C.W. Huang, Y.H. Su, Dynamic characteristics of partial composite beams, *International Journal of Structural Stability and Dynamics* 8 (2008) 665–685.
- [8] M. Dilena, A. Morassi, Vibrations of steel–concrete composite beams with partially degraded connection and applications to damage detection, *Journal of Sound and Vibration* 320 (2009) 101–124.
- [9] S. Berczynski, T. Wroblewski, Vibration of steel–concrete composite beams using the Timoshenko beam model, *Journal of Vibration and Control* 11 (2005) 829–848.
- [10] R. Xu, Y. Wu, Static, dynamic, and buckling analysis of partial interaction composite members using Timoshenko's beam theory, *International Journal of Mechanical Sciences* 49 (2007) 1139–1155.
- [11] J.R. Banerjee, C.W. Cheung, R. Morishima, M. Perera, J. Njuguna, Free vibration of a three-layered sandwich beam using the dynamic stiffness method and experiment, *International Journal of Solids and Structures* 44 (2007) 7543–7563.
- [12] M.E. Raville, E. Ueng, M. Lei, Natural frequencies of vibration of fixed–fixed sandwich beams, *ASME Journal of Applied Mechanics* 28 (1961) 367–371.
- [13] S. Chonan, Vibration and stability of sandwich beams with elastic bonding, *Journal of Sound and Vibration* 85 (1982) 525–537.
- [14] Y. Frostig, M. Baruch, Free vibrations of sandwich beams with a transversely flexible core: a high order approach, *Journal of Sound and Vibration* 176 (1994) 195–208.
- [15] H. Matsunaga, Vibration and buckling of multilayered composite beams according to higher order deformation theories, *Journal of Sound and Vibration* 246 (2001) 47–62.
- [16] D.J. Mead, A comparison of some equations for the flexural vibration of damped sandwich beams, *Journal of Sound and Vibration* 83 (1982) 363–377.
- [17] K. Chandrashekhar, K. Krisnamurthy, S. Roy, Free vibration of composite beams including rotary inertia and shear deformation, *Composite Structures* 14 (1990) 269–279.
- [18] S.J. Song, A.M. Waas, Effects of shear deformation on buckling and free vibration of laminated composite beams, *Composite Structures* 37 (1997) 33–43.
- [19] L. Jun, H. Hongxing, Free vibration analyses of axially loaded laminated composite beams based on higher-order shear deformation theory, *Meccanica*, 46 (2011) 1299–1317.
- [20] M. Tanveer, A.V. Singh, Linear and nonlinear dynamic responses of various shaped laminated composite plates, *ASME Journal of Computational and Nonlinear Dynamics* 4 (2009). 041011-1-13.
- [21] K.K. Teh, C.C. Huang, The vibration of generally orthotropic beams—a finite element approach, *Journal of Sound and Vibration* 62 (1979) 195–206.
- [22] H. Arvin, M. Sadighi, A.R. Ohadi, A numerical study of free and forced vibration of composite sandwich beam with viscoelastic core, *Composite Structures* 92 (2010) 996–1008.
- [23] W.P. Howson, A. Zare, Exact dynamic stiffness matrix for flexural vibration of three-layered sandwich beams, *Journal of Sound and Vibration* 282 (2005) 753–767.
- [24] V.S. Sokolinsky, H.F. von Bremen, J.A. Lavoie, S.R. Nutt, Analytical and experimental study of free vibration response of soft-core sandwich beams, *Journal of Sandwich Structures and Materials* 6 (2004) 239–261.
- [25] M.F. Aly, I.G.M. Goda, G.A. Hassan, Experimental investigation of the dynamic characteristics of laminated composite beams, *International Journal of Mechanical & Mechatronics Engineering* 10 (2010) 59–67.
- [26] M. Dilena, A. Morassi, A damage analysis of steel–concrete composite beams via dynamic methods. Part II: analytical models and damage detection, *Journal of Vibration and Control* 9 (2003) 529–565.
- [27] M. Dilena, A. Morassi, Experimental modal analysis of steel–concrete composite beams with partially damaged connection, *Journal of Vibration and Control* 10 (2004) 897–913.
- [28] R.A. Di Taranto, Theory of the vibratory bending for elastic and viscoelastic layered finite length beams, *ASME Journal of Applied Mechanics* 32 (1965) 881–886.
- [29] T. Sakiyama, H. Matsuda, C. Morita, Free vibration analysis of sandwich beam with elastic or viscoelastic core by applying the discrete Green function, *Journal of Sound and Vibration* 191 (1996) 189–206.
- [30] E.M. Kerwin, Damping of flexural waves by a constrained visco-elastic layer, *Journal of the Acoustical Society of America* 31 (1959) 952–962.
- [31] D.S. Ross, A. Cabal, D. Trauernicht, J. Lebens, Temperature-dependent vibrations of bilayer microbeams, *Sensors and Actuators A* 119 (2005) 537–543.
- [32] N. Ganesan, V. Pradeep, Buckling and vibration of sandwich beams with viscoelastic core under thermal environments, *Journal of Sound and Vibration* 286 (2005) 1067–1074.

- [33] N. Challamel, On lateral–torsional vibrations of elastic composite beams with interlayer slip, *Journal of Sound and Vibration* 325 (2009) 1012–1022.
- [34] E. Bozhevolnaya, J.Q. Sun, Free vibration analysis of curved sandwich beams, *Journal of Sandwich Structures and Materials* 6 (2004) 47–73.
- [35] V.S. Sokolinsky, S.R. Nutt, Y. Frostig, Boundary condition effects in free vibrations of higher-order soft sandwich beams, *AIAA Journal* 40 (2002) 1220–1227.
- [36] X. Shen, W. Chen, Y. Wu, R. Xu, Dynamic analysis of partial-interaction composite beams, *Composites Science and Technology* 71 (2011) 1286–1294.
- [37] J.D. Achenbach, *Wave Propagation in Elastic Solids*, North-Holland Publishing Company, 1973.